



HHS Public Access

Author manuscript

ACS Nano. Author manuscript; available in PMC 2018 June 17.

Published in final edited form as:

ACS Nano. 2017 February 28; 11(2): 2284–2303. doi:10.1021/acsnano.7b00609.

Thermal Decomposition Synthesis of Iron Oxide Nanoparticles with Diminished Magnetic Dead Layer by Controlled Addition of Oxygen

Mythreyi Unni[†], Amanda Uhl[‡], Shehaab Savliwala[†], Benjamin H. Savitzky[£], Rohan Dhavalikar[†], Nicolas Garraud^{||}, David P. Arnold^{||}, Lena F. Kourkoutis^{#,δ}, Jennifer Andrew[‡], and Carlos Rinaldi^{†,§,*}

[†]Department of Chemical Engineering, University of Florida, Gainesville, FL, 32611, USA

[‡]Department of Materials Science and Engineering University of Florida, Gainesville, FL, 32611, USA

[£]Department of Physics, Cornell University, Ithaca, NY, 14853, USA

[#]Applied & Engineering Physics, Cornell University, Ithaca, NY, 14853, USA

^δKavli Institute at Cornell for Nanoscale Science, Cornell University, Ithaca, NY, 14853, USA

^{||}Interdisciplinary Microsystems Group, Department of Electrical and Computer Engineering, University of Florida, Gainesville, FL, 32611, USA

[§]J. Crayton Pruitt Family Department of Biomedical Engineering, University of Florida, Gainesville, FL, 32611, USA

Abstract

Decades of research focused on size and shape control of iron oxide nanoparticles have led to methods of synthesis that afford excellent control over physical size and shape, but comparatively poor control over magnetic properties. Popular synthesis methods based on thermal decomposition of organometallic precursors in the absence of oxygen have yielded particles with mixed iron oxide phases, crystal defects and poorer than expected magnetic properties, including the existence of a thick “magnetically dead layer” experimentally evidenced by a magnetic diameter

*Corresponding Author: Corresponding author: carlos.rinaldi@bme.ufl.edu, Tel (352)-294-5588, Fax (352)-273-9221.

Author Contributions C.R and M.U conceived and designed the experiments. M.U performed the experiments and carried out all the physical and magnetic measurements. S.S performed the safety evaluation for oxygen addition and determined the factors for safe addition of molecular oxygen. B.H.S and L.F.K performed the HAADF-STEM measurements and analysed the data. N.G., R.D., D.P.A., and C.R. designed and built the instrumentation to characterize MPI properties of the nanoparticles; R.D performed and analysed the data from MPS/MPR measurements. J.A and A.U performed XRD on the samples and analyzed the data. All authors contributed to preparation of the manuscript. All authors have given approval to the final version of the manuscript.

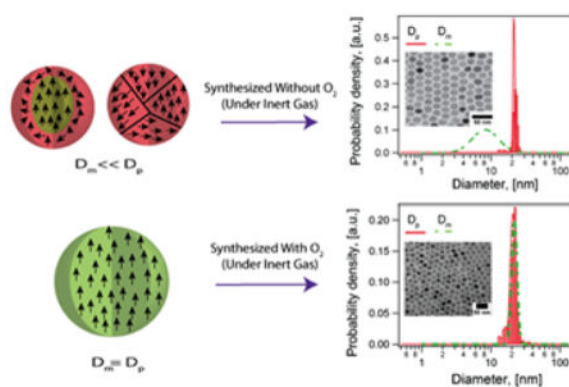
Notes

The authors declare no competing financial interest.

Supporting Information (SI). The SI includes has information on 1) Equilibrium Magnetization curves based on Langevin function 2) Size distributions of the commercial particle and 3,5) particles used for various applications 4) HAADF-STEM of additional single crystal particles synthesized in the presence of oxygen. 6,7) Plots related to analysis of AC susceptibility measurements as a function of temperature. 8) Size distributions of particle used to study heat dissipation and MPI properties 9) Relaxivity data of the particles. 10) Temperature profiles during reaction. Table S1 with particles synthesized under various conditions, Table S2 with details of exchange bias analysis, Table S3 and S4 with safety analysis performed for the addition of oxygen for the synthesis. This material is available free of charge *via* the Internet at <http://pubs.acs.org>.

significantly smaller than the physical diameter. Here, we show how single crystalline iron oxide nanoparticles with few defects and similar physical and magnetic diameter distributions can be obtained by introducing molecular oxygen as one of the reactive species in the thermal decomposition synthesis. This is achieved without the need for any post-synthesis oxidation or thermal annealing. These results address a significant challenge in the synthesis of nanoparticles with predictable magnetic properties and pave way to advances in applications of magnetic nanoparticles.

Graphical Abstract



Keywords

Iron oxide; magnetic nanoparticles; magnetic dead layer; oxygen; thermal decomposition; magnetic diameter

The past two decades have seen tremendous progress in the synthesis and applications of inorganic nanoparticles, motivated largely by the distinct properties they possess relative to their bulk counterparts. Much of this research has been driven by a desire to control and study nanoparticle physical, chemical, and electronic properties as a function of size and shape. As a result, a wide range of inorganic nanoparticles (*e.g.*, metal, metal oxide, semiconductor, *etc.*) can be synthesized with exquisite control over size (from single nm to 100s of nm) and shape (*e.g.*, spheres, rods *etc.*).¹⁻¹⁷ Synthesis methods involving the thermal decomposition of organometallic precursors in organic solvents with surfactant capping agents in an inert atmosphere provide a versatile platform for the synthesis of oxide-based nanoparticles, including magnetic nanoparticles. Control over the size, polydispersity, and shape of the nanoparticles has been achieved through thermal decomposition methods. However, because of safety concerns associated with the high temperatures of the organic liquid and vapor phases used in these reactions, they are typically carried out in conditions devoid of oxygen, leading to an apparent paradox: *If the reaction is carried out in the absence of oxygen, how can metal oxide nanoparticles be formed successfully and reproducibly?*

Magnetic nanoparticles are an important class of ferroic materials that exhibit a spontaneous magnetization that can be controlled by an applied magnetic field. In magnetic nanoparticles, one figure of merit is the saturation magnetization, which is related to the

strength of the nanoparticle's overall dipole moment, where high values can only be achieved when there is long range ordering of the atomic dipoles within the particle. Therefore, the presence of structural defects or impure phases will limit the overall performance of the nanoparticles.

Magnetic nanoparticles are attractive in a wide range of applications based on actuation of their magnetic dipoles using external fields or interaction of their magnetic dipoles with their surroundings.^{18,19} Interestingly, although the performance of iron oxide nanoparticles in many applications is critically dependent on their magnetic properties, these are often given cursory analysis in publications reporting improved methods of synthesis. Great attention is given to the physical size and shape of the nanoparticles, characterized using bright field transmission electron microscopy. Unfortunately, comparatively minimal effort is devoted to magnetic characterization.^{20–23} To date, an implicit assumption in the research community has been that magnetic properties scale directly with the physical diameter, as measured using transmission electron microscopy. When magnetic characterization is included in publications, it is often limited to demonstrating superparamagnetic behavior by noting the absence of coercivity/remanence and evaluating the saturation magnetization achieved at high applied magnetic fields.²⁴ In other cases, the temperature dependence of magnetization is reported through so-called “zero field cooled/field cooled” magnetization as a function of temperature, which yields the blocking temperature of the nanoparticles, indicative of the temperature above which a majority of the particles become superparamagnetic.^{25, 26} Unfortunately, even in publications that report such magnetic measurements, the data is rarely analyzed by comparing to available models and expectations. When magnetic properties, such as the saturation magnetization, are found to be poorer than expected, the result is often attributed to the existence of a “magnetically dead layer” on the surface of the nanoparticles, where spin canting and other phenomena may lead to disorder of the magnetic dipoles.^{27, 28} and this magnetic dead layer has often been attributed to cause the reduction in magnetic performance of the nanoparticles.^{29, 30} This is often the case even when the calculated thickness of the magnetically dead layer is found to be several nanometers thick, instead of the expected thickness of about one unit cell of the material.³¹

Thermal decomposition syntheses are quickly becoming the most common route to obtain magnetic nanoparticles. However, recent work has uncovered that the thermal decomposition routes may actually proceed by formation of a non-magnetic Wüstite phase and that formation of the magnetic magnetite/maghemite phases proceeds afterwards due to oxidation upon exposure to atmospheric oxygen.^{32–34} Furthermore, detailed high-resolution transmission electron microscopy studies suggest the presence of defects and polycrystalline particles, which may ultimately affect magnetic and functional properties of the nanoparticles.^{35, 36} This has led to the development of post-synthesis thermal oxidative treatments to improve the magnetic properties of the nanoparticles.^{37–39} However, while such treatments are successful for small (<15 nm) particles, they become less effective as particle size increases (>20 nm), or require extremely long (>30 h) processing times. This and other observations led us to hypothesize that lack of oxygen in the thermal decomposition reaction medium is a major obstacle for the reproducible synthesis of oxide-based nanoparticles through thermal decomposition.

Here, we report the reproducible synthesis of magnetic nanoparticles with similar physical and magnetic diameter distributions, and virtually no magnetically dead layer, without the need for post-synthesis modifications, through the incorporation of molecular oxygen as a reacting species in the thermal decomposition synthesis. Our results further show that the resulting nanoparticles consist of single crystals with few defects and possess magnetic properties consistent with those of bulk magnetite. As such, these results build towards reproducible synthesis of magnetic nanoparticles with predictable magnetic properties. This discovery is based on the judicious and careful reintroduction of molecular oxygen as a synthesis reagent during the high temperature thermal decomposition reaction.

The Magnetic Diameter – An Important but Often Neglected Property of Magnetic Nanoparticles

One way to quantify the magnetic properties of magnetic nanoparticles is to calculate an effective magnetic diameter distribution for a given sample. This can be achieved by fitting the superparamagnetic equilibrium magnetization curve of the nanoparticles to the Langevin function $L(\alpha)$ for superparamagnetism, weighted using a lognormal size suggested by Chantrell *et al.*⁴⁰

$$M(\alpha) = M_s \int_0^{\infty} n_v(D_m) L(\alpha) dD_m \quad (1)$$

$$n_v(D_m) = \frac{1}{\sqrt{2\pi} D_m \ln \sigma} \exp \left[-\frac{\ln^2 \left(\frac{D_m}{D_{mv}} \right)}{2 \ln^2 \sigma} \right] \quad (2)$$

$$L(\alpha) = \coth \alpha - \frac{1}{\alpha}; \alpha = \frac{\pi \mu_0 M_d D_m^3 H}{6 k_B T} \quad (3)$$

In equations (1)–(3), α is the Langevin parameter (the ratio of magnetic to thermal energy), M_s is the saturation magnetization of the sample consisting of a collection of magnetic nanoparticles in a non-magnetic medium, D_{mv} is the volume-weighted median magnetic diameter, $\ln \sigma$ is the geometric deviation of the magnetic diameter distribution, μ_0 is the permeability of free space, k_B is the Boltzmann constant, M_d is the domain magnetization of the magnetic nanoparticles, and T is the absolute temperature. The saturation magnetization is proportional to the domain magnetization multiplied by the volume fraction of magnetic nanoparticles in the sample. Fig. S1 in the Supporting Information illustrates the effects of D_{mv} and $\ln \sigma$ on the shape of the equilibrium magnetization curve. By fitting Eq. (1) to an equilibrium magnetization curve, one can obtain an estimate of the average magnetic diameter.

The possible existence of a nonmagnetic (or magnetically dead) layer on the surface of ferrite nanoparticles dates back to the work of Kaiser and Miskolczy³¹ who reported a model for the superparamagnetic magnetization curve that fit experimental data by allowing for the existence of a nonmagnetic layer that was one unit cell thick. Many recent studies that have compared magnetic and physical diameters have reported the magnetic diameters to be significantly smaller than the physical diameters, sometimes by several nanometers, an observation which is often attributed to the existence of a magnetically dead layer.^{27, 28, 30, 36, 41, 42–47} Similarly, some studies claim that surface modification of iron oxide nanoparticles can significantly influence the magnetic properties and change the thickness of the magnetically dead layer of the nanoparticles in a manner that depends on the specific interactions/bonding between the surface capping agent and the nanoparticle surface.⁴⁸ Post-synthesis oxidation and annealing have been shown to improve the magnetic diameter, but in most cases the magnetic diameter is still significantly smaller than the physical diameter for nanoparticles with large (>20 nm) physical diameters.^{44, 45} Recent work has shown that post-synthesis oxidation at elevated temperatures can reduce the thickness of the magnetically dead layer considerably, but only after prolonged periods of oxidation (>30 h).³⁹ Furthermore, a recent study showed that tuning the electrochemical potential of the solvent can influence the nature of the iron oxide phase obtained from synthesis.⁴⁹

Recent high-resolution electron microscopy studies suggest that iron oxide magnetic nanoparticles obtained by thermal decomposition may contain significant numbers of defects, and/or may consist of multiple crystals within a single particle.^{35, 36, 50, 51} While the effect on magnetic diameter distributions of such defects and/or presence of multiple crystals has not been reported, it is reasonable to expect that they could also contribute to a reduced magnetic diameter distribution relative to the physical size of the particles. For example, in the case of particles consisting of multiple crystal domains, one would expect the crystal domains to act as interacting magnetic dipoles whose overall diameter would necessarily be smaller than that of the overall particle. In such cases, the discrepancy between the magnetic diameter and physical diameter distributions would no longer be due to the existence of a magnetically dead layer in the sense introduced by Kaiser and Miskolczy³¹, but comparison of the two diameter distributions would still be useful as a characterization tool. In that case, one can think of an effective magnetically dead layer thickness that can serve as a simple figure of merit to evaluate the particle's magnetic properties.

From the perspective of applications of iron oxide nanoparticles, the observation of a magnetic diameter that is smaller than the physical diameter of the particles can be taken to imply that only a fraction of the nanoparticle's volume or mass contributes to a desired response. Alternatively, the observation that the magnetic diameter is smaller than the physical diameter can be taken to imply that the strength of the particle's dipole, and hence its response to applied fields, will be poorer than what would be expected based on physical size alone. Application-relevant properties such as the rate of energy dissipation used in nanoscale thermal cancer therapy,⁵² and magnetically-triggered drug release,⁵³ the magnetic forces relevant in ferrofluids,⁵⁴ magnetic capture,⁵⁵ magnetofection,⁵⁶ and signal intensity in magnetic particle imaging (MPI)⁵⁷ and magnetic resonance imaging (MRI)⁵⁸ are all expected to scale with the magnitude of the particle's magnetic dipoles, which in turn depend on the magnetic diameter distribution. Thus, methods that reduce or completely

eliminate the discrepancy between the magnetic and physical diameters of iron oxide magnetic nanoparticles would be extremely valuable for many applications. Here, we carry out experiments to demonstrate that addition of molecular oxygen during the thermal decomposition synthesis leads to particles with practically equal magnetic and physical diameters and with improved performance for various biomedical applications.

Results

Disparity between physical and magnetic diameter of iron oxide nanoparticles synthesized by thermal decomposition in the absence of oxygen and in commercial samples

Here, we illustrate the fact that current methods of thermal decomposition synthesis of magnetic nanoparticles in the absence of oxygen yield iron oxide nanoparticles with magnetic diameters that are significantly smaller than their physical diameters. To this end, iron oxide nanoparticles with relatively large (~20 nm) physical diameters were synthesized using the widely adopted heating up thermal decomposition synthesis of Park *et al.*⁵⁹ and the recently-reported semi-batch “Extended LaMer” synthesis of Vreeland *et al.*⁶⁰ Both methods consist of the thermal decomposition of an iron oleate precursor in a high boiling point solvent. In the heating-up synthesis, the iron oleate precursor is charged at room temperature, the reactor is closed, purged of oxygen, and the temperature is ramped to 320°C under an inert atmosphere and reflux. In the Extended LaMer synthesis, a reactor with an open neck and inert gas blanket is kept at a constant temperature (350°C) while the iron oleate precursor is added at a controlled rate. Specific details of how we synthesized the nanoparticles reported here are given under *Methods*. The resulting nanoparticles were characterized by transmission electron microscopy (TEM) and SQUID magnetometry. Physical diameter distributions were obtained from analysis of TEM images while magnetic diameter distributions were obtained from analysis of the equilibrium magnetization curves, as described under *Methods*.

As shown in Fig. 1, for both nanoparticle samples, the volume-weighted physical diameter distributions of iron oxide magnetic nanoparticles synthesized by the heating up and Extended LaMer thermal decomposition routes were found to be much larger than the volume-weighted magnetic diameter distributions. Particles synthesized by the heating up method (Fig. 1a) with nitrogen as an inert gas carrier resulted in a physical diameter D_p of 18.5 ± 1.7 nm and a much smaller magnetic diameter D_m of 10.7 ± 5.6 nm. This corresponds to a magnetically dead layer thickness of $\delta \sim 3.9$ nm. It is important to note in Fig. 1a that the physical size distribution is relatively narrow, with a coefficient of variation, CV, of 9%. In contrast, the magnetic size distribution is quite broad with CV = 52%. Similarly, particles obtained using the Extended LaMer mechanism thermal decomposition synthesis of iron oleate at 350°C in an argon atmosphere (Fig. 1b) had a physical diameter of 18.4 ± 1.1 nm (CV = 6%) and a magnetic diameter of 10.1 ± 5 nm (CV = 50%). In this case the magnetic dead layer thickness was $\delta \sim 4.1$ nm.

For comparison, and to demonstrate that the discrepancy between physical and magnetic diameter is not limited to our laboratory, samples of iron oxide nanoparticles with similar physical diameter were obtained from the commercial supplier Ocean Nanotech and subjected to the same analysis. As shown in Fig. 1c, commercially obtained iron oxide

nanoparticles from Ocean Nanotech had a physical diameter of 21.8 ± 1.95 nm (CV = 9%) and a magnetic diameter of 14.2 ± 4.9 nm (CV = 34%, $\delta \sim 3.8$ nm). Similar disparities between physical and magnetic diameters were found for nanoparticles from Ocean Nanotech in a wide range of physical diameters (see Fig. S2 in the Supporting Information). While we do not have access to the details by which this supplier produces their nanoparticles, their narrow size distribution is indicative of a thermal decomposition route. Furthermore, the results are relevant because commercially-available nanoparticles are adopted by many research groups working in applications of magnetic nanoparticles, but who lack expertise in magnetic nanoparticle synthesis and characterization.

Post synthesis modification can improve magnetic diameter

Particles synthesized by thermal decomposition methods in the absence of oxygen resulted in poor magnetic properties, evidenced by magnetic diameters that were smaller and had broader distributions than the physical diameter (Fig. 1). Others have reported an improvement in magnetic properties after post-synthesis thermal annealing and solution-phase oxidation.⁴⁵ However, while the magnetic diameter has been reported to increase with post-synthesis thermal annealing and oxidation, the effect of such treatments on the distribution of magnetic diameters has received limited attention. We therefore tested if such post-synthesis modification could result in improved magnetic diameter distributions.

Nanoparticles obtained by thermal decomposition in the absence of oxygen were heated to 120 °C for 2 hrs in octadecene post-synthesis, resulting in a slight increase in magnetic diameter. As shown in Fig. 2a, nanoparticles with a physical diameter of 15.8 ± 2.2 nm (CV = 14%) had a magnetic diameter of 8.1 ± 3.8 nm (CV = 47%) before thermal treatment and a magnetic diameter of 13.2 ± 0.9 nm (CV = 7%) after thermal treatment. Note that, not only did the magnetic diameter increase, but its distribution also became significantly narrower. However, there is still a significant magnetically dead layer, with a thickness of ~ 3.8 nm before thermal treatment and ~ 1.3 nm after thermal treatment. The limitations of post-synthesis thermal treatment are more evident when one considers much larger nanoparticles. Fig. 2b shows physical and magnetic diameter distributions for much larger iron oxide nanoparticles with a physical diameter of 26.0 ± 1.3 nm (CV = 5%). In this case the magnetic diameter was 12 ± 7.9 nm (CV = 65%) before thermal treatment and displayed a much smaller improvement to 15.4 ± 3 nm (CV = 19%) after thermal treatment. The thickness of the magnetically dead layer decreased only a little, from ~ 7 nm to ~ 5.3 nm. Thus, although thermal treatment again resulted in a narrowing of the magnetic size distribution, it appears to be much less effective in improving the overall magnetic diameter when the physical diameter of the nanoparticles is large. Furthermore, repeated trials under various thermal treatment conditions indicated that though thermal treatment showed evidence of higher magnetic diameter before and after oxidation, the method had poor reproducibility, particularly for larger particles. Finally, we note that a recent study demonstrated that high temperature oxidation post-synthesis yielded particles with similar physical and magnetic diameter distributions, however, the process takes over 30 h for large particles and requires optimization for each particle size.³⁹

Evidence of a role of atmospheric oxygen influx on the magnetic properties of nanoparticles obtained by the Extended LaMer synthesis

As the Extended LaMer synthesis reported by Vreeland *et al.*⁶⁰ uses an open reactor, we hypothesized that depending on the inert gas used, there could be diffusion of oxygen into the reaction medium. To test this hypothesis, we compared the use of argon and nitrogen as inert gases for the Extended LaMer synthesis in the absence of oxygen. Argon, being heavier than air, is expected to form an “inert blanket” on top of the reacting liquid, limiting oxygen transport into the reactor. As seen in Fig. 3a, nanoparticles obtained from this synthesis had a physical diameter of 24.6 ± 1.7 nm (CV = 7%) and a magnetic diameter of only 13.3 ± 6.3 nm (CV = 47%, $\delta \sim 5.6$ nm). For comparison, we synthesized nanoparticles using nitrogen as the inert gas. We hypothesized that nitrogen, being less dense than oxygen would allow molecular oxygen from the surrounding atmosphere to penetrate and dissolve into the reaction mixture, improving the magnetic diameter. Fig. 3b shows the physical and magnetic diameters for iron oxide nanoparticles obtained using conditions identical to those of Fig. 3a, with the substitution of nitrogen as the inert gas. The nanoparticles had a physical diameter of 24.1 ± 3.9 nm (CV = 16%) and a magnetic diameter of 18 ± 0.7 nm (CV = 4%, $\delta \sim 3$ nm). Interestingly, the physical diameters obtained using argon and nitrogen were very similar, but the magnetic diameter distribution of the nanoparticles obtained using nitrogen as the inert gas was larger and narrower than for those obtained using argon as the inert gas. This is consistent with the hypothesis that nitrogen as a carrier gas would allow more oxygen to enter the reactor. Regardless, although an improvement in magnetic diameter is observed using nitrogen as the carrier gas, the magnetic diameter is still significantly smaller than the physical diameter.

Effect of molecular oxygen as a reactant in the heating up thermal decomposition synthesis

Motivated by the observation that post-synthesis thermal oxidation led to significant relative improvement in magnetic diameter for small nanoparticles but not for larger nanoparticles, we surmised that *in situ* oxidation during synthesis would be advantageous. However, addition of molecular oxygen to the reactor presented a potential fire hazard if the gas-phase oxygen concentration exceeded the limiting oxygen concentration (LOC) given the temperature and pressure of the reactor headspace. We therefore reasoned that slow addition of molecular oxygen mixed with an inert carrier gas using a mass flow controller could be a viable option to introduce molecular oxygen as a reactive species in the thermal decomposition synthesis. For the heating-up synthesis, we further posited that molecular oxygen could be added to the reactor at several times the stoichiometrically required amount (determined from the mass of iron charged into the reactor), which could be delivered over the span of the synthesis.

Fig. 4 provides a comparison of the physical and magnetic diameters obtained for iron oxide nanoparticles synthesized using identical heating-up thermal decomposition syntheses, the only difference being the absence or presence of molecular oxygen supplied using a mass flow controller. As seen in Fig. 4a, nanoparticles synthesized in the absence of oxygen had a physical diameter of 18.5 ± 1.7 nm (CV = 9%) and a magnetic diameter of 10.7 ± 5.6 nm (CV = 52%, $\delta \sim 3.9$ nm). The controlled addition of oxygen at slight stoichiometric excess

to the reaction resulted in particles with physical diameter of 15.4 ± 1.9 nm (CV = 12.3%) and magnetic diameter of 14.1 ± 1.7 nm (CV = 12%, $\delta \sim 0.6$ nm), as seen in Fig. 4. Thus, introduction of oxygen in the heating-up thermal decomposition synthesis yielded particles with similar physical and magnetic diameters and a very thin magnetically dead layer, consistent with the expectation that this layer be about a unit cell in thickness.³¹

Controlled growth of physical and magnetic diameter in the Extended LaMer thermal decomposition synthesis through the controlled addition of molecular oxygen

An attractive feature of the semi batch synthesis using the Extended LaMer mechanism⁶⁰ is the ability to control the rate of growth and final nanoparticle size by controlling the rate at which the iron oleate precursor is added to the reaction and the total reaction time. We therefore hypothesized that if molecular oxygen is continuously added to the reaction, simultaneously with the iron oleate precursor and at a molar flow rate that is slightly above that required by the stoichiometry of magnetite, the nanoparticle's magnetic diameter would grow at the same rate as their physical diameter.

Fig. 5 and 6 compare the growth in physical and magnetic diameters with time in the Extended LaMer synthesis in the absence and in the presence of molecular oxygen, using argon as the inert carrier gas to minimize any effects of oxygen entering the reactor from the environment. For the synthesis in the absence of molecular oxygen and using argon as the inert gas (Fig. 5), the nanoparticles grew from 18.4 ± 1.1 nm (CV = 6%) to 26.4 ± 1.3 nm (CV = 5%) over a span of 5 hours, with corresponding magnetic diameters of 10.1 ± 5 nm (CV = 50%, $\delta \sim 4.1$ nm) to 15.7 ± 5.1 nm (CV = 32%, $\delta \sim 5.4$ nm). The fact that the thickness of the magnetically dead layer increases with time and growth of the nanoparticles indicates that the magnetic diameter is growing at a slower rate than the physical diameter. This would be consistent with our initial hypothesis that oxygen is a limiting reactant in the formation of the desired magnetic iron oxide phase. In contrast, when molecular oxygen was added at a controlled rate that was slightly above the stoichiometric rate required for the rate of addition of the iron oleate precursor, the physical and magnetic diameters were found to grow at similar rates. As shown in Fig. 6, the physical diameter increased from 13.6 ± 2.6 nm (CV=19%) to 18.3 ± 2.7 nm (CV=14%) while the magnetic diameter increased from 13.2 ± 2.5 nm (CV=19%, $\delta \sim 0.19$ nm) to 17.1 ± 1.7 nm (CV=10%, $\delta \sim 0.59$ nm). Thus, introduction of oxygen in the Extended LaMer thermal decomposition synthesis resulted in controlled growth of both physical and magnetic diameter and yielded particles with similar physical and magnetic diameters and a very thin magnetically dead layer, consistent with the expectation that this layer be about a unit cell in thickness.³¹

Table S1 in the Supplementary Information summarizes all the syntheses performed in the presence and absence of oxygen using both the heating up and the Extended LaMer method, showing the reproducibility in the results obtained.

Crystallite size from X-Ray diffraction studies agrees with magnetic diameters obtained from analysis of equilibrium magnetization curves

As noted previously, formation of Wüstite impurities in the thermal decomposition synthesis of iron oxide nanoparticles has been reported based on powder X-Ray diffraction (XRD)

data. We therefore tested if powder XRD of iron oxide nanoparticles synthesized using the heating-up and Extended LaMer syntheses in the absence and in the presence of molecular oxygen showed any evidence of the Wüstite phase. Fig. 7 shows the results, along with the expected peak locations and relative magnitudes for magnetite. The powder XRD patterns do not show any evidence of the wüstite phase and have peaks consistent with magnetite. However, detection of low (< 2–3%) mass fraction impurities using laboratory XRD is difficult and distinguishing the peaks of Wüstite and magnetite can be difficult, particularly for samples with broad peaks such as those obtained without the introduction of oxygen in the thermal decomposition synthesis. Furthermore, it is impossible to distinguish between magnetite and maghemite phases using XRD alone.^{61, 62}

Although the powder XRD data obtained for our samples does not show evidence of the Wüstite phase, we did observe that for syntheses in the absence of oxygen the peaks are broader than for syntheses in the presence of oxygen. One contributor to peak broadening in XRD is small crystallite size, hence this indicated that nanoparticles obtained through thermal decomposition in the absence of oxygen had smaller crystallite sizes than nanoparticles synthesized in the presence of oxygen. Because the origin of the nanoparticle's magnetic dipole is long range ferroic ordering in the crystal, we hypothesized that crystallite sizes obtained from fitting the powder XRD spectra of the nanoparticles using Scherrer's equation would correlate with the magnetic diameters determined from analysis of the equilibrium magnetization curves. Table 1 compares the physical D_p , magnetic D_m , and crystallite D_{XRD} sizes for the nanoparticles in Fig. 7. The standard deviations for the physical and magnetic diameters are also included, while no analog can be obtained for the crystallite size from analysis of the powder XRD data. Also, the lattice parameters remained unchanged for syntheses in the absence and presence of oxygen. Remarkably, the crystallite and magnetic sizes agree for all the nanoparticles, regardless of synthesis method and whether or not oxygen was present in the reaction, all three sizes are in reasonable agreement for nanoparticles synthesized in the presence of oxygen, and the crystallite size is smaller than the physical size for nanoparticles synthesized in the absence of oxygen.

Detailed structural characterization of the iron oxide nanoparticles using high-angle annular dark-field scanning transmission electron microscopy (HAADF-STEM)

While the physical size obtained from conventional TEM is larger than the magnetic size for particles synthesized in the absence of oxygen, the crystallite size obtained from XRD agrees with the magnetic size in all particles, synthesized both with and without oxygen present. However, the degree of crystallinity and local defect structures could not be determined directly with conventional TEM or XRD due to limited resolution. In order to unambiguously assess particle crystallinity and resolve the apparent disparities in measured physical size, magnetic size, and crystallite size, we performed high resolution scanning transmission electron microscopy in high-angle annular dark-field mode (HAADF-STEM), allowing detailed characterization of the local atomic structure, as shown in Fig. 8.

Here, we use HAADF-STEM to compare particles synthesized without and with oxygen having physical diameters of 21 ± 2 nm and 18 ± 1.1 nm, respectively, while their magnetic diameters determined from the Langevin fits were 12 ± 5.4 nm and 17 ± 1.7 nm,

respectively. The size distribution and conventional TEM images of the particles studied here may be found in Fig. S3 in the Supporting Information. The iron oxide nanoparticles synthesized in the absence of oxygen are found to be polycrystalline with locally defective, strained or tilted regions, shown in Fig. 8a. The particles synthesized in the presence of oxygen with comparatively equivalent physical and magnetic diameters were found to be consistently single crystalline, shown in Fig. 8b. Additional data supporting consistently single crystal structure is in Supporting Information, Fig. S4. In combination with the XRD data, these observations imply that polycrystallinity may be a crucial factor limiting magnetic properties in oxygen-free syntheses.

Effect of addition of molecular oxygen on fundamental magnetic properties

While our focus here has been to relate synthesis conditions and the influence of molecular oxygen in the reaction to the physical and magnetic diameter distributions, it is interesting to also consider if the addition of oxygen to the thermal decomposition reaction results in changes in other relevant magnetic properties of the nanoparticles. Here, we compare some of the most commonly studied magnetic properties for two iron oxide nanoparticle samples with similar physical diameter distributions obtained in the presence and absence of oxygen.

Saturation magnetization—The saturation magnetization is one of the most-often reported properties of magnetic nanoparticles, as it is a measure of the ultimate magnetization that can be obtained from a sample subjected to a high (saturating) magnetic field. In Fig. 9 we compare particles synthesized without (w/o) and with oxygen having physical diameters of 21 ± 2 nm and 21 ± 0.64 nm, respectively, but with magnetic diameters determined from the Langevin fits of 10 ± 5 nm and 20 ± 0.80 nm, respectively. The size distributions and the TEM images of the particles studied here may be found in Fig. S5 in the Supporting Information. When normalized by the nanoparticle concentration determined using the o-phenanthroline assay, the saturation magnetization of the particles synthesized in the absence of oxygen was found to be $17 \text{ Am}^2/\text{kg}$, whereas particles synthesized in the presence of oxygen had a saturation magnetization of $74 \text{ Am}^2/\text{kg}$. The bulk saturation magnetization value for magnetite is $86 \text{ Am}^2/\text{kg}$.⁶³ In a recent study reporting the post-synthesis oxidation of iron oxide nanoparticles obtained through a heating-up thermal decomposition synthesis, the authors reported saturation magnetization values in the range of $59\text{--}80 \text{ Am}^2/\text{kg}$ after >30 h of post-synthesis oxidation. In contrast, the nanoparticles reported here are obtained without any post-synthesis oxidation or annealing procedures.

Blocking temperature, ac susceptibility, and magnetic anisotropy—The temperature dependence of the magnetization of iron oxide nanoparticles is often reported as a means of evaluating the extent of their superparamagnetic character. This is typically done through zero field cooled (ZFC) and field cooled (FC) magnetization measurements from which the blocking temperature (the temperature corresponding to the peak of the zero field cooled magnetization curve) is taken to represent the temperature at which the nanoparticles transition from superparamagnetic to blocked magnetic behavior as temperature decreases. Alternatively, the blocking temperature can be used to estimate the magnetic anisotropy of

the nanoparticles, a measure of the energy barrier opposing switching of the magnetic dipoles between easy axes of the nanoparticle's crystal lattice.

ZFC and FC magnetization measurements for two nanoparticle samples are shown in Fig. 10. Here we compare particles synthesized without and with oxygen having physical diameters of 21 ± 2 nm and 18 ± 1.1 nm, respectively, but their magnetic diameters determined from the Langevin fits were 12 ± 5.4 nm and 17 ± 1.7 nm, respectively. The size distribution and the TEM images of the particles studied here may be found in Fig. S3 in the Supporting Information. The blocking temperatures were found to be 266.5 K and 98.2 K for the nanoparticles synthesized in the absence and presence of oxygen. Interestingly, even though the magnetic diameter was found to increase for the sample synthesized in the presence of oxygen, the blocking temperature was found to decrease. Also, the peak of the ZFC magnetization appears narrower for the nanoparticles synthesized in the presence of oxygen. We believe there are two contributors to these observations. First, we suspect that broadening of the magnetic diameter distribution for the sample synthesized in the absence of oxygen contributes to broadening of the ZFC magnetization peak. Second, we believe that the presence of more crystal defects in nanoparticles synthesized in the absence of oxygen, observed in HAADF-STEM images shown above, contribute to a higher magnetic anisotropy. Calculation of the magnetic anisotropy for each sample from the blocking temperature (see *Methods*) indicates that particles synthesized without oxygen had an anisotropy constant of 128 kJ/m^3 and 88 kJ/m^3 when determined using the Néel and Vogel-Fulcher models, respectively, whereas the anisotropy constant of the particles synthesized in the presence of oxygen was 20 kJ/m^3 and 8.5 kJ/m^3 respectively when determined using the Néel and Vogel-Fulcher models, respectively. The magnetic anisotropy values obtained for the nanoparticles synthesized in the presence of oxygen are close to the bulk value of 13.5 kJ/m^3 for magnetite.⁶⁴

An alternative method to estimate the magnetic anisotropy of the nanoparticles is to measure the temperature dependence of their ac susceptibility as a function of temperature for a range of applied magnetic field frequencies. The corresponding peak temperatures for each frequency are then plotted in a way that the anisotropy constant can be determined from the slope (see *Methods*). Measurements of the ac susceptibility for the same particles used in Fig. 10 are shown in Fig. 11. Corresponding plots used for analysis are shown in Fig. S6 and S7 in Supporting Information. As with the ZFC/FC magnetization measurements, we find that the ac susceptibility curves are narrower and have peaks at lower temperatures for the nanoparticles synthesized in the presence of oxygen. Similarly, we found that the magnetic anisotropy was lower for the nanoparticles synthesized in the presence of oxygen, even though their magnetic diameters were larger. For the particles synthesized in the absence of oxygen, the magnetic anisotropy was found to be 103 kJ/m^3 and 70 kJ/m^3 according to the Néel and Vogel-Fulcher models, whereas for the particles synthesized in the presence of oxygen the magnetic anisotropy was calculated to be 17 kJ/m^3 and 5.9 kJ/m^3 according to the Néel and Vogel-Fulcher models.

Evidence of exchange bias observed for nanoparticles synthesized in the absence of oxygen—Prior work has shown that formation of antiferromagnetic and ferromagnetic iron oxide phases in nanoparticles obtained by thermal decomposition

syntheses can be evaluated through characterization of exchange bias.³⁴ In such cases the presence of multiple magnetic phases within a particle can lead to magnetic disorder of the spins at the interface of two phases due to broken symmetry, roughness, and differences in stoichiometry from the bulk.⁶⁵ The extent of disorder can be evaluated by cooling the sample from above the Néel temperature of the antiferromagnetic phase in the particle in the presence of a field. The disordered spins would require higher magnetic energy than the ordered spins in the rest of the particle to align with the field, thereby resulting in a shifted hysteresis loop.

Fig. 12 a shows exchange bias measurements for particles synthesized in the absence of oxygen, with physical diameter of 21 ± 2.56 nm and magnetic diameter of 12 ± 5.4 nm. An asymmetry is observed for the coercive fields measured between 7 to -7 T and -7 to 7 T respectively, (Hc-1 and Hc-2) when compared to the corresponding ZFC (for which there should be no exchange bias). The coercive fields of the FC curves are higher than the coercive fields of the ZFC curves in the first cycle between 7 and -7 T as seen in the left panel. There is a shift in the hysteresis to the left for the FC magnetization curve as compared to the ZFC that is indicative of exchange bias. The coercive field shift decreases with repeating cycles as seen when the FC magnetization curves are compared to the ZFC magnetization curves between 7 and -7 T in the second cycle (right panel). The remanent magnetization is also higher for the first loop of the FC magnetization curve than for the ZFC magnetization curve when measured between 7 to -7 T. This effect also decreases when magnetization cycles are repeated, as may be seen when the FC and ZFC magnetization curves are compared between cycles.

Fig. 12b shows corresponding results for particles synthesized in the presence of oxygen, with physical diameter of 18 ± 2.5 nm and magnetic diameter of 17.1 ± 1.71 nm. In this case, no asymmetry is observed for the coercive fields measured between 7 to -7 T and -7 to 7 T respectively, (Hc-1 and Hc-2) when comparing the ZFC and FC magnetization curves in both cycles. Furthermore, the coercive fields of the FC magnetization curves are similar to the ZFC magnetization curves in the first cycle between 7 and -7 T, as seen in the left panel, and there is negligible shift between the ZFC and FC magnetization curves in both cycles. Finally, the remanent magnetization is similar for the FC and ZFC magnetization curves measured between 7 to -7 T and there is no shift in the remanent magnetization as cycles are repeated.

Table S2 in Supplementary Information summarizes the coercive fields (Hc) and the remanence magnetization (Mr) as obtained from these measurements. Taken together, these results suggest the existence of exchange bias in the nanoparticles synthesized in the absence of oxygen but not in the particles synthesized in the presence of oxygen.

Effect of addition of molecular oxygen on properties relevant to biomedical applications

Magnetic nanoparticles are of interest in several biomedical applications where the response of the nanoparticle's magnetic dipole to an applied time-varying or constant magnetic field plays a key role in performance. Here, we compare some of these application-relevant properties for two nanoparticle samples with similar physical diameter distributions but different magnetic diameter distributions, synthesized in the presence and absence of

oxygen. Specifically, we compare performance of these nanoparticles in terms of their ability to dissipate thermal energy in alternating magnetic fields (AMFs) and their image contrast properties for use in Magnetic Particle Imaging (MPI) and Magnetic Resonance Imaging (MRI).

As biomedical applications require dispersion of the nanoparticles in aqueous media, the nanoparticles were coated with poly(ethylene glycol) (PEG) using silane coupling agents, using procedures that have been reported to yield nanoparticles with excellent colloidal stability in water and biological buffers.⁶⁶ The resulting particles have similar physical diameters of 21.2 ± 2.64 nm and 20.45 ± 1.64 nm but have a magnetic diameter of 12 ± 5.4 nm (synthesized in the absence of oxygen) and 17 ± 1.7 nm (synthesized in the presence of oxygen). After coating with PEG the particles synthesized in the presence had a hydrodynamic diameter, D_H , of 47 ± 3 nm, while those synthesized in the absence of oxygen had $D_H = 56 \pm 4$ nm. We did not observe any evidence of particle aggregation during any of the studies reported below. The size distributions, TEM images, and Langevin fits of the particles studied here may be found in Fig. S8 in the Supplementary Information. We note that prior to coating with PEG-silane, the nanoparticles synthesized in the presence of oxygen had similar magnetic and physical diameter distributions. Others have reported changes in magnetic properties due to changes in surface coating of magnetic nanoparticles.⁴⁸ We aim to further explore this possibility in future work.

Thermal energy dissipation in alternating magnetic fields—The energy dissipation rate of the particles, quantified as specific absorption rate (SAR), was determined under identical conditions and at a field amplitude of 10 kA/m and frequency of 343 kHz for samples with an iron concentration of 1 mg_{Fe}/mL. The corresponding temperature profiles are compared in Fig. 13. The particles synthesized in the presence of oxygen had a SAR of 209 W/gFe, approximately three times higher than the SAR of the particles synthesized in the absence of oxygen (84 W/gFe). Perhaps more importantly, when the SAR was normalized by the frequency and square of the magnitude of the applied AMF, the resulting Intrinsic Loss Power (ILP) value was found to be 6.1 nHm²/kg for the nanoparticles synthesized in the presence of oxygen and 2.4 nH m²/kg for the nanoparticles synthesized in the absence of oxygen. ILP values allow comparison of energy dissipation rates across laboratories using different instrumentation to generate the AMF.⁶⁷ In two recent surveys of the ILP values of commercial and laboratory nanoparticles, Pankurst and collaborators⁶⁸ have reported ILP values that range from 0.17 to 3.12 nH m²/kg, whereas in a paper by Merida *et al.*,⁶⁹ a review of the literature also found that most ILP values were below ~5 nH m²/kg, with some exceptional ILP values of 5.7 nHm²/kg for iron oxide nanocubes, 4.7 nH m²/kg for bacterial magnetosomes, and 5.9 nHm²/kg for maghemite nanoflowers. This illustrates how the addition of oxygen as a reactive species in the thermal decomposition synthesis leads to significant improvements in the ability of the nanoparticles to dissipate thermal energy in AMFs. Ongoing work aims to correlate magnetic diameter with energy dissipation rate and obtain nanoparticles with optimal properties for application in hyperthermia and magnetically-triggered drug release.

Magnetic Particle Imaging (MPI) performance—MPI is an emerging biomedical imaging technology where image contrast is provided solely by magnetic nanoparticles in a specimen.^{70, 71} As such, MPI is considered as a form of molecular imaging with potential spatial and temporal resolution that rivals nuclear imaging techniques, without the need of radioactive tracers.^{72, 73} There are currently two forms of MPI: (1) Harmonic Space MPI, developed by Philips, and (2) X-Space MPI, developed at the University of California, Berkeley. For Harmonic Space MPI the imaging performance of magnetic nanoparticles is determined on the basis of the harmonic spectrum of their response to an oscillating magnetic field, obtained using a magnetic spectrometer.⁷⁴ In X-Space MPI, the imaging performance of magnetic nanoparticles is determined from the point spread function (PSF), obtained using a magnetic relaxometer.⁷⁵ Here we compare the Harmonic Space and X-Space MPI performance of the PEG-coated nanoparticles synthesized in the presence and absence of oxygen used in the energy dissipation measurements described above. Fig. 14 summarizes the results of measurements in a custom-built magnetic spectrometer/relaxometer. For the Harmonic Space MPI characterization we report the Fast Fourier Transform of the sample signal in response to an applied oscillating magnetic field of 30 mT and 24 kHz. For the X-Space MPI characterization we report the PSF obtained using the methods reported by Goodwill and Conolly⁷⁶ for an excitation field amplitude of 30 mT and frequency of 24 kHz, with a bias field ramped from -100 mT to 100 mT over a period of 1s. In both cases the sample response has been normalized by the iron content, to enable direct comparisons. Considering Fig. 14a, the particles synthesized in the presence of oxygen exhibit better Harmonic Space MPI performance compared to particles synthesized in the absence of oxygen, as evidenced by the higher signal amplitude for all harmonics and a slower rate of decay of the harmonic spectrum. Considering Fig. 14b, the nanoparticles synthesized in the presence of oxygen also exhibit better X-Space MPI performance, as evidenced by greater signal strength (39.0 a.u. mL/mgFe vs 13.1 a.u. mL/mgFe). Additionally, the corresponding full width at half maximum (FWHM) values were of 12.0 mT for the nanoparticles synthesized in the presence of oxygen and 15.2 mT for the nanoparticles synthesized in the absence of oxygen. Lower FWHM values are associated with improved resolution in MPI,⁷³ indicating that addition of oxygen to the thermal decomposition reaction leads to particles with potential for higher resolution imaging. For comparison, typical FWHM values reported recently for similar field conditions range from 4.7–11.1 mT.^{77, 78} Ongoing work aims to correlate magnetic diameter to nanoparticle performance for MPI and obtain nanoparticles with performance that approaches theoretical predictions.⁷⁹

Magnetic Resonance Imaging (MRI) performance—Magnetic nanoparticles provide contrast for MRI by distorting the magnetic field in their vicinity, affecting the response of water protons to pulsed magnetic fields superimposed with a constant magnetic field that can be 1.7 T or more depending on the instrument.⁸⁰ This distortion of the local magnetic field surrounding the nanoparticles translates primarily into a change in the so-called transverse (T2) relaxation time and corresponding relaxivity.⁸⁰ We measured the MRI longitudinal (T1) and transverse (T2) relaxivities for the iron oxide nanoparticles coated with PEG-silane particles when synthesized in the presence ($D_H = 47 \pm 3$ nm) and absence of oxygen ($D_H = 56 \pm 4$ nm), and compared these to those of ferucarbotran ($D_m = 10.5 \pm 7.2$ nm, $D_H = 30$ nm

according to our measurements), the non-GMP form of the clinically-approved MRI contrast agent resovist. The corresponding plots of relaxivity as a function of concentration are shown in Fig. S9 in the Supporting Information.

The longitudinal (R_1) relaxivity of the ferucarbotran nanoparticles was found to be 3.35 [mMs]^{-1} , whereas for the particles synthesized in the presence and absence of oxygen it was found to be 0.31 and 0.34 [mMs]^{-1} , respectively. The corresponding transverse (R_2) relaxivities were found to be very similar for all three samples (175.3 [mMs]^{-1} for ferucarbotran, 166.5 [mMs]^{-1} for nanoparticles synthesized in the presence of oxygen, and 167.2 [mMs]^{-1} for nanoparticles synthesized in the absence of oxygen. The ratio of transverse to longitudinal relaxivities (R_2/R_1) is a measure of the efficiency of T2 or so-called “negative” contrast agents. This was found to be similar for the particles synthesized in the presence and absence of oxygen (536 and 497, respectively), both of which were higher than the value for ferrucarbotran (52). Interestingly, our results appear to indicate that introduction of oxygen into the thermal decomposition reaction, with corresponding increase in magnetic diameter for a given physical diameter, does not seem to lead to improvements in the MRI contrast properties of the nanoparticles. We believe that this is because of the relatively strong constant magnetic field in an MRI scanner, which would effectively saturate the magnetic nanoparticles regardless of their magnetic diameter distribution.

Discussion

It is evident from the results presented above that the magnetic diameter of iron oxide nanoparticles synthesized by conventional thermal decomposition routes and obtained from commercial suppliers such as Ocean Nanotech are significantly lower, and often significantly broader, than the corresponding physical diameters obtained from observation by transmission electron microscopy. Post-synthesis thermal and oxidative treatment was found to have limited benefits in terms of increasing the magnetic diameter. After post-synthesis oxidation, the magnetic diameter of the nanoparticles was found to increase and the polydispersity was found to narrow. However, the relative increase in magnetic diameter appeared to be less significant for larger nanoparticles, and a significant difference remained between the physical and magnetic diameters after treatment.

Particles synthesized in an open reactor system using the Extended LaMer mechanism based synthesis in the absence of molecular oxygen and using argon as the inert gas yielded particles with larger differences between physical and magnetic diameter distributions than when nitrogen was used as the inert gas. We believe that in an open reaction system, argon forms a dense blanket that prevents atmospheric oxygen from reaching the reaction mixture. In contrast, nitrogen, being less dense, allows for the diffusion of oxygen from the atmosphere, thus resulting in nanoparticles with slightly larger magnetic diameters. Nevertheless, the magnetic size distribution remained broad and physical and magnetic diameters were significantly different, suggesting the existence of a thick magnetically dead layer. The observation that switching argon and nitrogen gases leads to changes in the magnetic diameter is illustrative of how seemingly minor differences in synthesis protocol can lead to profound differences in the magnetic properties of the nanoparticles.

Taken together, the observations summarized above led us to hypothesize that the key to obtaining iron oxide nanoparticles with equal physical and magnetic diameters could be to oxidize the nanoparticles *in situ* during their synthesis and growth. The results of experiments where we synthesized iron oxide nanoparticles by both the heating up and extended LaMer mechanism based synthesis in the absence and presence of molecular oxygen were consistent with this hypothesis. We found that the physical and magnetic diameters of nanoparticles synthesized in the presence of molecular oxygen were found to be nearly identical, in contrast to cases where nanoparticles were synthesized in the absence of molecular oxygen. In fact, in all cases the thickness of the magnetically dead layer was found to be consistent with the expectation that it corresponds to about a single unit cell,³¹ and negligible compared to the diameter of the particles. The fact that addition of molecular oxygen worked to improve magnetic diameters in both synthesis schemes is also supportive of our earlier stated hypothesis that traditionally these reactions are carried out under conditions where oxygen is the limiting reactant. We also observed that for samples synthesized in the absence of O₂, the magnetic diameter of samples left exposed to atmosphere was found to increase over a span of 3 months' indicative of particle oxidation with time. Whereas the magnetic diameter of the particles synthesized in the presence of oxygen remained unaltered over the period of time thus assuring that required oxide phase is obtained at the time of synthesis itself. Furthermore, we have found that the thermal decomposition synthesis of iron oxide nanoparticles in the presence of molecular oxygen is highly reproducible in terms of physical and magnetic diameters, at least in comparison with our earlier experience with thermal decomposition synthesis in the absence of molecular oxygen. We believe this may be due to slight differences in residual oxygen in the reactor, which are difficult to control when the reaction is carried out in an "inert" atmosphere. Such residual oxygen may significantly influence the initial nucleation step, affecting the initial number of nuclei and thereby the final size that can be achieved for a given mass of iron oleate precursor. Indeed, a recent publication reported that reducing the amount of residual oxygen in the thermal decomposition synthesis of cobalt ferrite resulted in larger particle sizes.⁸¹ We believe that this observation is likely due to formation of fewer nuclei under reduced residual oxygen. In contrast, when molecular oxygen is added throughout the reaction, the overall concentration of oxygen can be ensured to be nearly the same across synthesis batches, resulting in greater reproducibility in physical size of the resulting nanoparticles (in addition to the improved magnetic diameters reported herein). Further efforts to understand the role of molecular oxygen on the nucleation event in the extended LaMer mechanism based synthesis are underway.

Our XRD results clearly demonstrate the presence of an iron oxide phase in the synthesized particles, but no evidence of a Wüstite impurity. While there is no definitive evidence of iron oxide phase impurities in the XRD data, this could be attributed to the concentration of the non-magnetic phases being below the detectable limit for XRD or the width of the peaks for the samples synthesized in the absence of oxygen. However, analysis of powder XRD patterns to obtain crystallite sizes is consistent with the expectation that crystallite size and magnetic diameter should be correlated, as the magnetic dipole of the nanoparticles arises due to long-range crystal ordering. As shown in Table 1, the crystallite sizes calculated using Scherrer's equation and the powder XRD patterns match the magnetic diameters of all

particles tested, regardless of synthesis method or the presence of oxygen. Furthermore, only for the case of nanoparticles synthesized in the presence of oxygen do the physical, magnetic, and crystallite sizes agree. In contrast, for nanoparticles synthesized in the absence of oxygen the crystallite size is smaller than the physical diameter.

HAADF-STEM revealed the detailed local crystal structure of the particles (Fig. 8). STEM data showed the particles synthesized in the absence of oxygen are polycrystalline, which is consistent with the observed disparities in physical diameter obtained by conventional TEM, magnetic diameter obtained by SQUID measurements, and crystallite diameter measured by XRD in these samples. STEM data further showed that particles synthesized in the presence of oxygen were single crystalline, consistent with physical, magnetic, and crystallite diameters which all agree.

Detailed magnetic and application-relevant characterization for selected samples demonstrated that the introduction of molecular oxygen into the thermal decomposition reaction yielded particles with basic magnetic properties (saturation magnetization and magnetic anisotropy) that are close to those expected for bulk magnetite and with narrower distributions (such as in the ZFC/FC and ac susceptibility measurements in Fig. 10 and 11), indicative of more uniform magnetic properties. Evidence of exchange bias effect was observed for nanoparticles synthesized in the absence of oxygen, but not for particles synthesized in the presence of oxygen (Fig. 12). Taken together, these observations suggest that use of oxygen as a reactant during the thermal decomposition synthesis leads to nanoparticles with magnetic properties expected of single domain/single crystal iron oxide. We believe that this translated to the improved performance of the nanoparticles synthesized in the presence of oxygen for applications that rely on time-varying magnetic fields, such as in thermal energy dissipation and magnetic particle imaging (Fig. 13 and Fig. 14), where a larger magnetic diameter can translate to a stronger response of the particles to the time-varying magnetic field. Furthermore, we believe that the narrower magnetic diameter distributions of the nanoparticles synthesized in the presence of oxygen also contribute to improved performance. Indeed, in the context of thermal energy dissipation by magnetic nanoparticles the negative impact of broadening of the size distribution is well documented,⁸² but as far as we know this has exclusively been interpreted to be due to distribution in the physical size of the nanoparticles while the effect of the distribution of magnetic diameter is commonly ignored. Finally, in addition to promising improvements in the energy dissipation rates and magnetic particle imaging performance, the ability to tune both the physical and magnetic diameter using molecular oxygen as a reactive species in the thermal decomposition synthesis is particularly exciting for development of magnetic nanoparticles with optimal performance in a wide range of biomedical applications.

Conclusions

The studies reported here demonstrate the critical role that molecular oxygen plays in determining the magnetic properties of iron oxide nanoparticles obtained through thermal decomposition syntheses. Experiments carried out in “inert” atmospheres using argon and nitrogen as inert blanket and carrier gases demonstrated that the resulting particles possessed magnetic diameter distributions that were smaller and broader than the corresponding

physical diameter distributions. Further, experiments with post-synthesis oxidation demonstrated that while an improvement in magnetic diameter distributions can be obtained with such methods, this improvement is difficult to control and limited for larger particles. Our results demonstrate that the safe and judicious addition of molecular oxygen as a species in the thermal decomposition synthesis leads to nanoparticles with practically equal physical and magnetic diameter distributions, magnetic properties that resemble those expected for bulk magnetite, and improved application-relevant properties such as thermal energy dissipation rate and resolution for magnetic particle imaging. Of particular relevance, our observations suggest that addition of oxygen as a reactant during the thermal decomposition synthesis yields nanoparticles that are uniformly single crystalline, whereas synthesis in the absence of oxygen yields nanoparticles that are consistently polycrystalline. Beyond the ability to obtain nanoparticles with tuned physical and magnetic diameters, our results suggest that an important contributor to the wide range of magnetic and functional properties in the literature may be due to the discrepancies in the magnetic diameter distribution of nanoparticles obtained by thermal decomposition routes in the absence of oxygen. It is therefore our hope that the methods reported here will lead to more thorough magnetic characterization of nanoparticles developed for biomedical applications, as well as improved size-structure-property relationships for magnetic nanoparticles.

Methods

IMPORTANT: Safety considerations in the addition of molecular oxygen to the thermal decomposition synthesis

Thermal decomposition syntheses are typically carried out at temperatures well above the flash point of the organic vapors generated by the reaction mixture. As such, these reactions are typically carried out under anaerobic conditions. Therefore, safety considerations are paramount when adding molecular oxygen to a thermal decomposition reaction. An important realization here is that the amount of oxygen needed to achieve stoichiometric ratios with respect to the iron typically used in a thermal decomposition synthesis is actually quite small, hence one can envision adding the oxygen at a low enough rate such that the risk of flashing of the organic vapors is minimized. An important concept here is that of the Limiting Oxygen Concentration (LOC), which is the minimum O₂ concentration in a mixture of fuel, air, and an inert gas that will propagate flame. In the absence of guidelines for the LOC in mixtures containing compositions such as the ones used in the thermal decomposition synthesis, we opted to maintain inert gas flow rates such that if no molecular oxygen was consumed in the synthesis of the nanoparticles the head space oxygen concentration would be low.⁸³ Theoretical rates of combustion of various organic solvents as a function of rate of oxygen addition were calculated to identify safe addition flow rates during synthesis (see Supplementary Information, Section II). Based on the molar flow rate at which iron is added in the synthesis by Extended LaMer mechanism based synthesis, we calculated that the flow rate of a 21% oxygen in nitrogen mixture required to achieve stoichiometric ratios between iron and oxygen was 2.35 sccm (standard cubic centimeters per minute). However, we decided to use a slight excess of 4 times the stoichiometric flow rate in order to promote *in-situ* oxidization of the nanoparticles. Inert carrier gas was also

added at a rate of 100 sccm, keeping the net oxygen concentration in the inlet gas stream well below 5%.

Synthesis of Iron oleate precursor for the heating up thermal decomposition route

The iron oleate precursor was prepared according to the method developed by Park et.al.⁵⁹ Briefly, 7.557 g of iron chloride hexahydrate [Fe(Cl₃)·6H₂O, ACS reagent, >97% pure from Sigma] was dissolved in 42 mL of water and reacted with 25.66 g of sodium oleate [97%, TCI America] in 98 mL hexane and 56 mL ethanol in a 500 mL 3 neck reactor. The reaction under nitrogen atmosphere was mixed using a Caframo compact overhead stirrer at 200 RPM. The reaction mixture was heated to about 60 °C using a fabric heating mantle (115 V, from GlasCol) and temperature control was ensured using a Digi-sense temperature controller (EW-89000-00, 120V, 15 A) for 4 hrs. Iron oleate formed was purified by repeated washes with deionized water and further dried of solvents using a rotary evaporator at 60 °C oil bath at 11 mbar for 30min at 45 rpm. The oleate was aged for 15 days before being used for the thermal decomposition synthesis.

To confirm the formation of the iron (III) oleate and characterize the functional groups present, infrared spectra were collected using a Nicolet 6700 FTIR spectrometer (Thermo Scientific). The detected intensity after total internal reflection was analyzed using OMNIC software to generate a spectrum of absorbance vs wavenumber (cm⁻¹). The sample was scanned from 4000 to 600 cm⁻¹ at 4 cm⁻¹ resolution.

Magnetic nanoparticle synthesis by the heating up thermal decomposition route in the absence of oxygen

Iron oxide nanoparticles were synthesised by reacting 23.13 g of the iron oleate obtained using the method of Park *et al.*⁵⁹ with 7.3 g of oleic acid in 128.21 mL of trioctylamine as the non-reacting solvent in a 500 mL three neck reactor. The reaction in the presence of nitrogen controlled by a mass flow controller (Alicat Scientific) at 100 sccm as the carrier gas was ramped up to 340°C at 3.3°C/min under reflux. In all cases, particles obtained at the end of 1 hr were purified by hexane and acetone washes.

Synthesis of iron oleate precursor for the Extended LaMer thermal decomposition route

A stoichiometrically defined iron oleate was prepared according to the method developed by Vreeland et.al⁶⁰ to be used in the Extended LaMer mechanism based synthesis. Briefly, 20.02 g (56.7 mmol) of iron acetylacetonate [Fe(acac)₃] >98% pure, TCI America] and 80 g (283.5 mmol) of oleic acid (90% technical grade, Sigma Aldrich) were charged into a 500 mL three neck reactor flask. The reaction under 100 sccm of Argon was thoroughly mixed using a Caframo compact overhead stirrer at 350 RPM. The reaction mixture was heated to about 320°C at a ramp rate of 8°C/min using a fabric heating mantle and temperature was controlled using a Digi-sense temperature controller. After 35 minutes at 320°C, a dark brown waxy solid was obtained and used as the precursor for the Extended LaMer mechanism based synthesis after 24 hours.

Magnetic nanoparticle synthesis by the Extended LaMer thermal decomposition route in the absence of oxygen

14.015 g (48.3 mmol) of docosane (90% pure, Sigma Aldrich), was initially heated to 350°C for 50–60 min at a ramp rate of 7–8 °C/min in a 100 mL three neck reaction flask. The rate of addition of inert gas was controlled using mass flow controllers from Alicat Scientific. Once the reactor reached 350°C the controlled addition (using a syringe pump) of 30 mL of iron oleate precursor (0.63 M Fe) mixed with 55 mL of 1-octadecene (90% technical grade, Sigma Aldrich) was initiated. Uniform mixing at 350 RPM was ensured and the reaction temperature was controlled at 350°C for 5 hrs using a Digi-sense temperature controller. To understand the kinetics involved, aliquots of 1–2 mL were withdrawn using Pasteur pipettes at regular intervals. The reaction mixture was allowed to cool to room temperature and iron-oxide nanoparticles obtained at the end of the reaction were purified by suspending 5 mL of the black waxy liquid in 10–20 mL of hexane. The particles were precipitated using 20–40 mL of acetone by centrifuging in an Eppendorf 5430R at 7500 RPM for 10 minutes.

Post synthesis oxidation of iron oxide nanoparticles

In order to improve the magnetic properties, particles suspended in organic solvents were thermally treated at 120°C with and without bubbling air for particles synthesized by Extended LaMer Mechanism.

Oxidation by bubbling in air—Approximately 15 mg/mL of iron oxide particles were suspended in 2 mL of oleic acid and placed in a heating block from Fisher for 4 hrs at 120°C with air being bubbled in the samples. There was significant color change of the sample from dark brown to light brown and high rates of oleic acid boil off were observed.

Oxidation by solvent transfer without bubbling in air—Approximately 5 mg of as-synthesized iron oxide nanoparticles were suspended in 2 mL hexane and sonicated for 10 minutes. Further 2 mL of 1-octadecene was added to the vial and the particles left in an oven for 2 hrs at 120°C. The particles remained well suspended in 1-octadecene and color change was observed during oxidation.

Magnetic nanoparticle synthesis by the heating up thermal decomposition route in the presence of oxygen

For syntheses carried out using molecular oxygen, the conditions were the same as described above for syntheses in the absence of oxygen, but oxygen feed of 20% Oxygen and 80% Ar (Airgas) was added to the reactor at a rate of 9.47 sccm, controlled using a mass flow controller (Bronkhorst USA), starting when the reaction reached 340 °C and lasting until the end of the reaction.

Magnetic nanoparticle synthesis by the Extended LaMer thermal decomposition route in the presence of oxygen

For syntheses carried out using molecular oxygen the conditions were the same as described above for syntheses by extended LaMer mechanism in the absence of oxygen, except that oxygen feed of 20% Oxygen and 80% Ar (Airgas) was added to the reactor at a rate of 9.47

sccm, controlled using a mass flow controller (Bronkhorst USA), simultaneously with the addition of the iron oleate precursor throughout the reaction.

Quantification of Fe in particle samples

10 μL of Oleic acid or PEG coated iron oxide particles suspended in toluene and water respectively were digested in 70% conc. HNO_3 (Optima Grade, Fisher Scientific) and left overnight at 101°C in a heating dry block. 10 μL of digested sample was dried and iron in 46 μL in water was further reduced with 30 μL hydroxylamine hydrochloride (8.06 M) for 1hr. 75 μL of 1,10-phenanthroline monohydrate (13 mM) was added to complex with Fe^{2+} , promoted using 49 μL sodium acetate (1.22 M). Absorbance of the 100 μL samples was measured at 508 nm in a SpectraMax M5 Microplate reader. The concentration of each sample run in triplicate was determined by relating to a calibration curve prepared using iron standard solutions prepared from a FLUKA Iron Standard for ICP.

Characterization of SPIONS

Physical size distributions—Physical diameters (D_p) of the oleic acid coated particles were obtained by imaging using a Hitachi H 7000 Transmission Electron Microscope (TEM). Images of particles sampled on an Ultrathin Carbon Type A (3–4nm) with removable formvar grid from TedPella were acquired using a Veleta CCD side mount camera and were analyzed using ImageJ.⁸⁴

The number median diameter (D_{pg}) and geometric deviation ($\ln\sigma_g$) of the particle size distribution were obtained by fitting the size distribution histograms to the lognormal distribution

$$n_N(D_p) = \frac{1}{\sqrt{2\pi}D_p \ln \sigma_g} \exp\left(-\frac{\ln^2(D_p/D_{pg})}{2 \ln^2 \sigma_g}\right) \quad (4)$$

The number median diameter (D_{pg}) was converted to a volume median diameter (D_{pgv}) using

$$D_{pgv} = \exp\left(\ln D_{pg} + 3 \ln^2 \sigma_g\right) \quad (5)$$

The arithmetic volume mean diameter (D_{pv}) and sigma (σ) were calculated using

$$D_{pv} = \exp\left(\ln D_{pgv} + \frac{\ln^2 \sigma_g}{2}\right) \quad (6)$$

$$\sigma = D_{pv} \sqrt{\exp(\ln^2 \sigma_g) - 1} \quad (7)$$

Magnetic size distributions—A Quantum Design Magnetic Property Measurement System 3 (MPMS 3) Superconducting Quantum Inference Device (SQUID) magnetometer was used to study the intrinsic properties of the oleic acid coated magnetic nanoparticles synthesized. Magnetization curves at room temperature were obtained for liquid samples in a PTFE sample holder with 100 μ L of iron-oxide nanoparticles suspended in hexane/water. The volume-weighted median magnetic diameter (D_{mv}) and geometric deviation of the magnetic nanoparticle samples were determined by fitting the superparamagnetic equilibrium magnetization curve to the Langevin function, weighted using a lognormal size distribution $n_v(D_m)$, as commonly done in the literature.^{28,40,85,86} Two important assumptions are made in this analysis: the magnetic domains are spherical and the magnetic domains possess a magnetization equal to that of bulk magnetite (446,000 A/m). The corresponding equations are (1) to (3) and the volume median diameter obtained was converted to volume mean using equation (6). The saturation magnetization was deduced from the maximum of the magnetization obtained from the magnetization curves.

Crystal structure and crystallite size—X-ray powder diffractograms were collected using a Panalytical Xpert powder diffractometer with Cu-K-alpha radiation (45 kV, 40 mA) and a scintillation detector. Rietveld refinement was performed using High Score Plus on the obtained patterns and the crystallite size in each phase was estimated using Scherrer's formula. Phase was determined by matching the diffraction peaks of the sample with those in a database obtained from the International Center for Diffraction Data.

HAADF STEM—The high resolution STEM images were acquired using a NION UltraSTEM100, with lens aberrations corrected up to and including 5th order. An operating voltage of 100keV, a convergence angle of 30 mrad, and an inner detector angle of 80 mrad were used. Each STEM image was obtained by cross-correlating and averaging over 3–5 image acquisitions.

Thermal energy dissipation in alternating magnetic fields—Heat dissipated by the particles was quantified as Specific Absorption Rate (SAR). About 200 μ L of 1 mg Fe/mL of PEG coated particles suspended in water was placed in a custom made induction coil at field strength of 10 kA/m and a frequency of 343 kHz. An alternating magnetic field (AMF) was generated in the coil by using an Ambrell EASYHEAT 8130LI 10 kW induction heater. The temperature of the coil and sample were monitored by fiber-optic temperature probe from Neoptix. SAR was calculated from the initial rise in temperature with time deduced from above calorimetric measurements using

$$SAR \left(\frac{W}{g_{Fe}} \right) = \frac{C_p}{m_{Fe}} * \frac{\Delta T}{\Delta t} * m_{sample} \quad (8)$$

where, C_p is the heat capacity of the solvent, and $\Delta T/\Delta t$ is the initial rate of temperature rise.

Blocking temperature and magnetic anisotropy—To study the blocking temperature, magnetic anisotropy constant and the interaction temperature, iron oxide nanoparticles suspended in octadecene were immobilized in polystyrene divinyl benzene (PSDVB) at 0.02 wt. % of iron wherein the particle rotation was fixed. Initial susceptibility of the particles was estimated from magnetization curves measured between 4 and 400 K at field ramp of 0.001 T/min at a low field strength of 10 Oe. A plot of the inverse of initial susceptibility and temperature was fitted to the Curie-Weiss model as given by equation (9), to obtain interaction temperature, a parameter that accounts for extent of magnetic dipole interaction in the sample.

$$\chi_0 = \frac{A}{(T - T_0)} \quad (9)$$

The anisotropy constant was determined from the dynamic response of the particle to oscillating magnetic field of 10 Oe amplitude over a range of temperatures (4 to 400 k) at different frequencies in the range of 0.1 to 1000 kHz. The Néel model ($T_0 = 0$) and the Volger-Fulcher model modified to account for the polydispersity of the sample as given in equation (10) is used to interpret the temperature dependence of the Dynamic Magnetic Susceptibility measurements. From the plot of $\ln(1/\Omega)$ versus $1/T$, the slope provides an estimate of KV_m and the infinite temperature intercept gives measure of τ_0

$$\ln \frac{1}{\Omega} = \ln \tau_0 + \left(\frac{KV_m}{k_B(T - T_0)} \right) \exp\left(\frac{9}{2} \ln \sigma_g^2\right) \quad (10)$$

Zero Field Cooled-Field Cooled (ZFC-FC) measurements were made to evaluate the blocking temperature (T_B) obtained from the maximum of the ZFC curves. The magnetization of the sample was measured at a constant field of 10 Oe were in the temperature was swept at 2 K/min from 10 K to 400 K in ZFC measurements and cooled to 10 K from 400 K in the FC measurements. The anisotropy constant was found using equation (11) from the Néel relaxation model ($T_0 = 0$) and the Volger-Fulcher model that was modified to account for the polydispersity of the sample.

$$K = \frac{k_B(T_B - T_0)}{V_m} \ln \left(\frac{\tau_{obs}}{\tau_0} \right) \frac{1}{\exp(9/2 \ln^2 \sigma_g)} \quad (11)$$

where the characteristic time τ_0 was found from the inverse frequency of the applied oscillating magnetic field vs temperature obtained from the ac susceptibility measurements and the observation time (τ_{obs}) being the sweep rate by the blocking temperature.

Evaluation of exchange bias effect—Evaluating the presence of exchange bias in a magnetic nanoparticle sample, such as may be due to magnetic ordering of the spins at the interface of a ferromagnetic and antiferromagnetic phase, is often performed by low temperature magnetic analysis where the sample is cooled from above the Néel temperature of the antiferromagnetic phase in the presence of a magnetic field. Dilute samples embedded in PSDVB (so as to minimize particle-particle interactions) were cooled to 5 K from 298 K in the presence of a 7 T magnetic field, after which field cooled (FC) magnetization curves were measured in the field range 7 T to -7 T using a SQUID magnetometer. Zero field cooled (ZFC) magnetization curves were obtained after cooling the sample in the absence of a field. A shift in the hysteresis along the field and changes in the coercivity and remanence were used to characterize the extent of exchange bias in the samples. We also studied the so-called training effect, wherein increasing numbers of hysteresis loops at the same temperature lead to a decrease in the exchange bias effect and concomitantly in the shift of the hysteresis curve.⁸⁷

Magnetic Particle Imaging (MPI) performance—A magnetic particle relaxometer (MPR)⁸⁸ or magnetic particle spectrometer (MPS)⁸⁹ is often used to assess the performance of tracers in MPI. A custom-built MPS/MPR instrument at the University of Florida was used to measure the response of particles to a sinusoidal and ramped sinusoidal magnetic field, in order to characterize their performance for Magnetic Particle Imaging. 1 mL PEG-coated particles in centrifuge tubes were excited at an amplitude of 30 mT and frequency of 24 kHz for MPS measurements and in MPR measurements exposed to a ramped sinusoidal field produced as a combination of a bias field (100 mT) and sinusoidal drive field (30 mT, 24kHz). The signal (induced voltage) recorded in the pickup coil during MPS measurement was further transformed into a harmonic spectrum through Fast Fourier Transform, whereas the signal from MPR measurements was transformed into a point spread function (PSF) using the x-space reconstruction formulation.⁷⁶ The harmonic spectrum and PSF was normalized by the iron concentration determined from o-phenanthroline assay by UV spectrophotometry.

Magnetic Resonance Imaging (MRI) performance—T1 and T2 relaxivity measurements were carried out using an Agilent 4.7 T magnetic resonance imaging system. 200 μ L of iron oxide nanoparticle of Fe concentration ranging from 0.1– 1 mM Fe was loaded in the PCR tubes and placed inside the bore of the magnet. The operating parameters for T1 inversion recovery were $T_R = 18$ s, $T_E = 7.11$ ms (60 times), matrix size = 256*128, and Field of View = 60*35, slide thickness = 2 mm and for the T2 measurements were $T_R = 18$ s, $T_E = 5.5$ ms (60 times), matrix size = 256*128, and Field of View = 60*35. A linear fit to plots of the inverse of relaxation time (T1 and T2) [1/s] vs concentration [mMFe] was used to estimate the relaxivity (R1 and R2) in [mMs]⁻¹ for all particles.

Supplementary Material

Refer to Web version on PubMed Central for supplementary material.

Acknowledgments

We thank the University of Florida for providing support and infrastructure during the course of research. This work was supported in part by NIH grants R01AR068424 and R21EB018453. We are grateful to Lorena Maldonado for useful insights on the synthesis of iron oxide nanoparticles using the heating up method. A portion of this work was performed in the McKnight Brain Institute at the National High Magnetic Field Laboratory's AMRIS Facility, which is supported by National Science Foundation Cooperative Agreement No. DMR-1157490 and the State of Florida. The work at Cornell was supported by the David and Lucile Packard Foundation and made use of the Cornell Center for Materials Research Shared Facilities which are supported through the NSF MRSEC program (DMR-1120296). B.H.S. was supported by NSF GRFP grant DGE-1144153.

References

1. Cheng G, Walker ARH. Synthesis and Characterization of Cobalt/gold Bimetallic Nanoparticles. *J Magn Magn Mater*. 2007; 311:31–35.
2. Cheon JW, Kang NJ, Lee SM, Lee JH, Yoon JH, Oh SJ. Shape Evolution of Single-Crystalline Iron Oxide Nanocrystals. *J Am Chem Soc*. 2003; 125:6553–6557. [PubMed: 12785795] 2004; 126:1950–1951.
3. Eustis S, El-Sayed MA. Why Gold Nanoparticles are More Precious Than Pretty Gold: Noble Metal Surface Plasmon Resonance and its Enhancement of the Radiative and Nonradiative Properties of Nanocrystals of Different Shapes. *Chem Soc Rev*. 2006; 35:209–217. [PubMed: 16505915]
4. Gerion D, Pinaud F, Williams SC, Parak WJ, Zanchet D, Weiss S, Alivisatos AP. Synthesis and Properties of Biocompatible Water-soluble Silica-coated CdSe/ZnS Semiconductor Quantum Dots. *J Phys Chem B*. 2001; 105:8861–8871.
5. Joo J, Yu T, Kim YW, Park HM, Wu FX, Zhang JZ, Hyeon T. Multigram Scale Synthesis and Characterization of Monodisperse Tetragonal Zirconia Nanocrystals. *J Am Chem Soc*. 2003; 125:6553–6557. [PubMed: 12785795]
6. Jun YW, Choi JS, Cheon J. Shape Control of Semiconductor and Metal Oxide Nanocrystals Through Nonhydrolytic Colloidal Routes. *Angew Chem, Int Ed*. 2006; 45:3414–3439.
7. Kim D, Lee N, Park M, Kim BH, An K, Hyeon T. Synthesis of Uniform Ferrimagnetic Magnetite Nanocubes. *J Am Chem Soc*. 2009; 131:454–455. [PubMed: 19099480]
8. O'Brien S, Brus L, Murray CB. Synthesis Of Monodisperse Nanoparticles Of Barium Titanate: Toward A Generalized Strategy Of Oxide Nanoparticle Synthesis. *J Am Chem Soc*. 2001; 123:12085–12086. [PubMed: 11724617]
9. Park J, Joo J, Kwon SG, Jang Y, Hyeon T. Synthesis Of Monodisperse Spherical Nanocrystals. *Angew Chem, Int Ed*. 2007; 46:4630–4660.
10. Perez MD, Otal E, Bilmes SA, Soler-Illia G, Crepaldi EL, Grosso D, Sanchez C. Growth of Gold Nanoparticle Arrays in TiO₂ Mesoporous Matrixes. *Langmuir*. 2004; 20:6879–6886. [PubMed: 15274599]
11. Penner RM. Mesoscopic Metal Particles and Wires by Electrodeposition. *J Phys Chem*. 2002; 106:3339–3353.
12. Rao CNR, Matte HSSR, Voggu R, Govindaraj A. Recent Progress in the Synthesis of Inorganic Nanoparticles. *Dalton Trans*. 2012; 41:5089–5120. [PubMed: 22430878]
13. Sun SH, Zeng H, Robinson DB, Raoux S, Rice PM, Wang SX, Li GX. Monodisperse MFe₂O₄ (M = Fe, Co, Mn) Nanoparticles. *J Am Chem Soc*. 2004; 126:273–279. [PubMed: 14709092]
14. Yin Y, Alivisatos AP. Colloidal Nanocrystal Synthesis and the Organic-Inorganic Interface. *Nature*. 2005; 437:664–670. [PubMed: 16193041]
15. Yu WW, Falkner JC, Yavuz CT, Colvin VL. Synthesis of Monodisperse Iron Oxide Nanocrystals by Thermal Decomposition of Iron Carboxylate Salts. *Chem Commun (Cambridge, U K)*. 2004:2306–2307.
16. Yu X, Chen K. A Facile Surfactant-Free Fabrication of Single-Crystalline Truncated Fe₃O₄ Cubes. *Mater Sci Eng, B*. 2011; 176:750–755.
17. Tao AR, Habas S, Yang P. Shape Control of Colloidal Metal Nanocrystals. *Small*. 2008; 4:310–325.

18. Pankhurst QA, Thanh NTK, Jones SK, Dobson J. Progress in Applications of Magnetic Nanoparticles in Biomedicine. *J Phys D: Appl Phys.* 2009;42.
19. Laurent S, Forge D, Port M, Roch A, Robic C, Elst LV, Muller RN. Magnetic Iron Oxide Nanoparticles: Synthesis, Stabilization, Vectorization, Physicochemical Characterizations, and Biological Applications. *Chem Rev.* 2008; 108:2064–2110. [PubMed: 18543879]
20. Gao GH, Liu XH, Shi RR, Zhou KC, Shi YG, Ma RZ, Takayama-Muromachi E, Qiu GZ. Shape-Controlled Synthesis and Magnetic Properties of Monodisperse Fe₃O₄ Nanocubes. *Cryst Growth Des.* 2010; 10:2888–2894.
21. Hyeon T. Chemical Synthesis of Magnetic Nanoparticles. *Chem Commun (Cambridge, U K).* 2003:927–934.
22. Belaid S, Laurent S, Vermeesch M, Vander Elst L, Perez-Morga D, Muller RN. A New Approach to Follow the Formation of Iron Oxide Nanoparticles Synthesized by Thermal Decomposition. *Nanotechnology.* 2013:24.
23. Bronstein LM, Huang X, Retrum J, Schmucker A, Pink M, Stein BD, Dragnea B. Influence of Iron Oleate Complex Structure on Iron Oxide Nanoparticle Formation. *Chem Mater.* 2007; 19:3624–3632.
24. Mahdavi M, Bin Ahmad M, Haron MJ, Namvar F, Nadi B, Ab Rahman MZ, Amin J. Synthesis, Surface Modification and Characterisation of Biocompatible Magnetic Iron Oxide Nanoparticles for Biomedical Applications. *Molecules.* 2013; 18:7533–7548. [PubMed: 23807578]
25. Woo K, Hong J, Choi S, Lee HW, Ahn JP, Kim CS, Lee SW. Easy Synthesis And Magnetic Properties of Iron Oxide Nanoparticles. *Chem Mater.* 2004; 16:2814–2818.
26. Guardia P, Labarta A, Batlle X. Tuning the Size, the Shape, and the Magnetic Properties of Iron Oxide Nanoparticles. *J Phys Chem C.* 2011; 115:390–396.
27. Morales MP, Veintemillas-Verdaguer S, Montero MI, Serna CJ, Roig A, Casas L, Martinez B, Sandiumenge F. Surface and Internal Spin Canting in Gamma-Fe₂O₃ Nanoparticles. *Chem Mater.* 1999; 11:3058–3064.
28. Luijckes B, Woudenberg SMC, de Groot R, Meeldijk JD, Galvis HMT, de Jong KP, Philipse AP, Erne BH. Diverging Geometric and Magnetic Size Distributions of Iron Oxide Nanocrystals. *J Phys Chem C.* 2011; 115:14598–14605.
29. Lieberma L, Clinton J, Edwards DM, Mathon J. Dead Layers in Ferromagnetic Transition Metals. *Phys Rev Lett.* 1970; 25:232.
30. Baaziz W, Pichon BP, Fleutot S, Liu Y, Lefevre C, Greneche JM, Toumi M, Mhiri T, Begin-Colin S. Magnetic Iron Oxide Nanoparticles: Reproducible Tuning of the Size and Nanosized-Dependent Composition, Defects, and Spin Canting. *J Phys Chem C.* 2014; 118:3795–3810.
31. Kaiser R, Miskolcz G. Magnetic Properties of Stable Dispersions of Subdomain Magnetite Particles. *J Appl Phys.* 1970; 41:1064.
32. Chalasani R, Vasudevan S. Form, Content, and Magnetism in Iron Oxide Nanocrystals. *J Phys Chem C.* 2011; 115:18088–18093.
33. Pichon BP, Gerber O, Lefevre C, Florea I, Fleutot S, Baaziz W, Pauly M, Ohlmann M, Ulhaq C, Ersen O, Pierron-Bohnes V, Panissod P, Drillon M, Begin-Colin S. Microstructural and Magnetic Investigations of Wustite-Spinel Core-Shell Cubic-Shaped Nanoparticles. *Chem Mater.* 2011; 23:2886–2900.
34. Casula MF, Jun YW, Zaziski DJ, Chan EM, Corrias A, Alivisatos AP. The Concept of Delayed Nucleation in Nanocrystal Growth Demonstrated for the Case of Iron Oxide Nanodisks. *J Am Chem Soc.* 2006; 128:1675–1682. [PubMed: 16448141]
35. Wetterskog E, Tai CW, Grins J, Bergstrom L, Salazar-Alvarez G. Anomalous Magnetic Properties of Nanoparticles Arising from Defect Structures: Topotaxial Oxidation of Fe_{1-x}O vertical bar Fe₃-delta O₄ Core vertical bar Shell Nanocubes to Single-Phase Particles. *ACS Nano.* 2013; 7:7132–7144. [PubMed: 23899269]
36. Levy M, Quarta A, Espinosa A, Figuerola A, Wilhelm C, Garcia-Hernandez M, Genovese A, Falqui A, Alloyeau D, Buonsanti R, Davide Cozzoli P, Angel Garcia M, Gazeau F, Pellegrino T. Correlating Magneto-Structural Properties to Hyperthermia Performance of Highly Monodisperse Iron Oxide Nanoparticles Prepared by a Seeded-Growth Route. *Chem Mater.* 2011; 23:4170–4180.

37. Panchal V, Bhandarkar U, Neergat M, Suresh KG. Controlling Magnetic Properties Of Iron Oxide Nanoparticles Using Post-Synthesis Thermal Treatment. *Appl Phys A: Mater Sci Process*. 2014; 114:537–544.
38. Sun SH, Zeng H. Size-Controlled Synthesis Of Magnetite Nanoparticles. *J Am Chem Soc*. 2002; 124:8204–8205. [PubMed: 12105897]
39. Kemp SJ, Ferguson RM, Khandhar AP, Krishnan KM. Monodisperse Magnetite Nanoparticles with Nearly Ideal Saturation Magnetization. *RSC Adv*. 2016; 6:77452–77464.
40. Chantrell RW, Popplewell J, Charles SW. Measurements of Particle-Size Distribution Parameters in Ferrofluids. *IEEE Trans Magn*. 1978; 14:975–977.
41. Gonzales-Weimuller M, Zeisberger M, Krishnan KM. Size-Dependant Heating Rates of Iron Oxide Nanoparticles for Magnetic Fluid Hyperthermia. *J Magn Magn Mater*. 2009; 321:1947–1950. [PubMed: 26405373]
42. Issa B, Obaidat IM, Albiss BA, Haik Y. Magnetic Nanoparticles: Surface Effects and Properties Related to Biomedicine Applications. *Int J Mol Sci*. 2013; 14:21266–21305. [PubMed: 24232575]
43. van Rijssel J, Kuipers BWM, Erne BH. Bimodal Distribution of the Magnetic Dipole Moment in Nanoparticles with a Monomodal Distribution of the Physical Size. *J Magn Magn Mater*. 2015; 380:325–329.
44. Chen R, Christiansen MG, Anikeeva P. Maximizing Hysteretic Losses in Magnetic Ferrite Nanoparticles *via* Model-Driven Synthesis and Materials Optimization. *ACS Nano*. 2013; 7:8990–9000. [PubMed: 24016039]
45. Hufschmid R, Arami H, Ferguson RM, Gonzales M, Teeman E, Brush LN, Browning ND, Krishnan KM. Synthesis of Phase-Pure And Monodisperse Iron Oxide Nanoparticles By Thermal Decomposition. *Nanoscale*. 2015; 7:11142–11154. [PubMed: 26059262]
46. Parkin SSP, Sigsbee R, Felici R, Felcher GP. Observation of Magnetic Dead Layers At The Surface Of Iron-Oxide Films. *Appl Phys Lett*. 1986; 48:604–606.
47. Jang SY, You CY, Lim SH, Lee SR. Annealing Effects on the Magnetic Dead Layer and Saturation Magnetization in Unit Structures Relevant to a Synthetic Ferrimagnetic Free Structure. *J Appl Phys*. 2011; 109:5.
48. Kandasamy G, Maity D. Recent advances in Superparamagnetic Iron Oxide Nanoparticles (SPIONS) For *In Vitro* And *In Vivo* Cancer Nanotheranostics. *Int J Pharm*. 2015; 496:191–218. [PubMed: 26520409]
49. Chen R, Christiansen MG, Sourakov A, Mohr A, Matsumoto Y, Okada S, Jasanoff A, Anikeeva P. High-Performance Ferrite Nanoparticles through Nonaqueous Redox Phase Tuning. *Nano Lett*. 2016; 16:1345–1351. [PubMed: 26756463]
50. Estrader M, Lopez-Ortega A, Golosovsky IV, Estrade S, Roca AG, Salazar-Alvarez G, Lopez-Conesa L, Tobia D, Winkler E, Ardisson JD, Macedo WAA, Morphis A, et al. Origin of the Large Dispersion of Magnetic Properties in Nanostructured Oxides: FexO/Fe3O4 Nanoparticles As A Case Study. *Nanoscale*. 2015; 7:3002–3015. [PubMed: 25600147]
51. Torruella P, Arenal R, de la Pena F, Saghi Z, Yedra L, Eljarrat A, Lopez-Conesa L, Estrader M, Lopez-Ortega A, Salazar-Alvarez G, Nogues J, et al. 3D Visualization of the Iron Oxidation State in FeO/Fe3O4 Core-Shell Nanocubes from Electron Energy Loss Tomography. *Nano Lett*. 2016; 16:5068–5073. [PubMed: 27383904]
52. Creixell M, Bohorquez AC, Torres-Lugo M, Rinaldi C. EGFR-Targeted Magnetic Nanoparticle Heaters Kill Cancer Cells without a Perceptible Temperature Rise. *ACS Nano*. 2011; 5:7124–7129. [PubMed: 21838221]
53. Bonini M, Berti D, Baglioni P. Nanostructures for Magnetically Triggered Release of Drugs and Biomolecules. *Curr Opin Colloid Interface Sci*. 2013; 18:459–467.
54. Torres-Diaz I, Rinaldi C. Recent Progress in Ferrofluids Research: Novel Applications of Magnetically Controllable and Tunable Fluids. *Soft Matter*. 2014; 10:8584–8602. [PubMed: 25277700]
55. Wang Y, Jia HZ, Han K, Zhuo RX, Zhang XZ. Theranostic Magnetic Nanoparticles for Efficient Capture and *In Situ* Chemotherapy of Circulating Tumor Cells. *J Mater Chem B*. 2013; 1:3344–3352.

56. Mykhaylyk O, Antequera YS, Vlaskou D, Plank C. Generation of Magnetic Nonviral Gene Transfer Agents and Magnetofection In Vitro. *Nat Protoc.* 2007; 2:2391–2411. [PubMed: 17947981]
57. Ferguson RM, Khandhar AP, Kemp SJ, Arami H, Saritas EU, Croft LR, Konkle J, Goodwill PW, Halkola A, Rahmer J, Borgert J, Conolly SM, et al. Magnetic Particle Imaging With Tailored Iron Oxide Nanoparticle Tracers. *IEEE Trans Med Imaging.* 2015; 34:1077–1084. [PubMed: 25438306]
58. Li L, Jiang W, Luo K, Song H, Lan F, Wu Y, Gu Z. Superparamagnetic Iron Oxide Nanoparticles as MRI Contrast Agents for Non-Invasive Stem Cell Labeling and Tracking. *Theranostics.* 2013; 3:595–615. [PubMed: 23946825]
59. Park J, An KJ, Hwang YS, Park JG, Noh HJ, Kim JY, Park JH, Hwang NM, Hyeon T. Ultra-Large-Scale Syntheses of Monodisperse Nanocrystals. *Nat Mater.* 2004; 3:891–895. [PubMed: 15568032]
60. Vreeland EC, Watt J, Schober GB, Hance BG, Austin MJ, Price AD, Fellows BD, Monson TC, Hudak NS, Maldonado-Camargo L, Bohorquez AC, Rinaldi C, Huber DL. Enhanced Nanoparticle Size Control by Extending LaMer's Mechanism. *Chem Mater.* 2015; 27:6059–6066.
61. Roca AG, Marco JF, del Puerto Morales M, Serna CJ. Effect of Nature and Particle Size on Properties of Uniform Magnetite and Maghemite Nanoparticles. *J Phys Chem C.* 2007; 111:18577–18584.
62. Mamani JB, Gamarra LF, de Souza Brito GE. Synthesis and Characterization of Fe₃O₄ Nanoparticles with Perspectives in Biomedical Applications. *Mat Res.* 2014; 17:542–549.
63. Cornell, RM., Schwertmann, U. The iron oxides: structure, properties, reactions, occurrence, and uses. VCH; Weinheim; New York: 1996. Electronic, Electrical and Magnetic Properties and Colour; p. 118
64. Birks JB. The Properties of Ferromagnetic Compounds at Centimetre Wavelengths. *Proc Phys Soc London, Sect B.* 1950; 63:65–74.
65. Phan, Manh-Huong, Alonso, Javier, Khurshid, H., Lampen-Kelley, P., Chandra, S., Repa, KS., Nemati, Z., Das, R., Iglesias, Ó., Srikanth, H. Exchange Bias Effects in Iron Oxide-Based Nanoparticle Systems. *Functional Magnetic Nanoparticles in Nanomedicine. Nanomaterials.* 2016; 6:221.
66. Barrera C, Herrera AP, Rinaldi C. Colloidal Dispersions of Monodisperse Magnetite Nanoparticles Modified with Poly(Ethylene Glycol). *J Colloid Interface Sci.* 2009; 329:107–113. [PubMed: 18930466]
67. Kallumadil M, Tada M, Nakagawa T, Abe M, Southern P, Pankhurst QA. Suitability of Commercial Colloids for Magnetic Hyperthermia. *J Magn Magn Mater.* 2009; 321:1509–1513.
68. Wildeboer RR, Southern P, Pankhurst QA. On the Reliable Measurement of Specific Absorption Rates and Intrinsic Loss Parameters in Magnetic Hyperthermia Materials. *J Phys D: Appl Phys.* 2014:47.
69. Merida F, Chiu-Lam A, Bohorquez A, Maldonado-Camargo L, Perez ME, Pericchi L, Torres-Lugo M, Rinaldi C. Optimization of Synthesis and Peptization Steps to Obtain Iron Oxide Nanoparticles with High Energy Dissipation Rates. *J Magn Magn Mater.* 2015; 394:361–371. [PubMed: 26273124]
70. Panagiotopoulos N, Duschka RL, Ahlborg M, Bringout G, Debbeler C, Graeser M, Kaethner C, Ludtke-Buzug K, Medimagh H, Stelzner J, Buzug TM, Barkhausen J, Vogt FM, Haegele J. Magnetic Particle Imaging: Current Developments and Future Directions. *Int J Nanomed.* 2015:10.
71. Bauer LM, Situ SF, Griswold MA, Samia ACS. Magnetic Particle Imaging Tracers: State-of-the-Art and Future Directions. *J Phys Chem Lett.* 2015; 6:2509–2517. [PubMed: 26266727]
72. Gleich B, Weizenecker R. Tomographic Imaging Using the Nonlinear Response Of Magnetic Particles. *Nature.* 2005; 435:1214–1217. [PubMed: 15988521]
73. Goodwill PW, Saritas EU, Croft LR, Kim TN, Krishnan KM, Schaffer DV, Conolly SM. X-Space MPI: Magnetic Nanoparticles for Safe Medical Imaging. *Adv Mater News.* 2012; 24:3870–3877.
74. Biederer S, Knopp T, Sattel TF, Ludtke-Buzug K, Gleich B, Weizenecker J, Borgert J, Buzug TM. Magnetization Response Spectroscopy of Superparamagnetic Nanoparticles for Magnetic Particle Imaging. *J Phys D: Appl Phys.* 2009:42.

75. Goodwill PW, Tamrazian A, Croft LR, Lu CD, Johnson EM, Pidaparathi R, Ferguson RM, Khandhar AP, Krishnan KM, Conolly SM. Ferrohydrodynamic Relaxometry for Magnetic Particle Imaging. *Appl Phys Lett*. 2011;98.
76. Goodwill PW, Conolly SM. The X-Space Formulation of the Magnetic Particle Imaging Process: 1-D Signal, Resolution, Bandwidth, SNR, SAR, and Magnetostimulation. *IEEE Trans Med Imaging*. 2010; 29:1851–1859. [PubMed: 20529726]
77. Arami H, Khandhar AP, Tomitaka A, Yu E, Goodwill PW, Conolly SM, Krishnan KM. *In Vivo* Multimodal Magnetic Particle Imaging (MPI) with Tailored Magneto/Optical Contrast Agents. *Biomaterials*. 2015; 52:251–261. [PubMed: 25818431]
78. Khandhar AP, Ferguson RM, Arami H, Kemp SJ, Krishnan KM. Tuning Surface Coatings of Optimized Magnetite Nanoparticle Tracers for *In Vivo* Magnetic Particle Imaging. *IEEE Trans Magn*. 2015:51.
79. Dhavalikar R, Maldonado-Camargo L, Garraud N, Rinaldi C. Ferrohydrodynamic Modeling of Magnetic Nanoparticle Harmonic Spectra for Magnetic Particle Imaging. *J Appl Phys*. 2015:118.
80. Na HB, Song IC, Hyeon T. Inorganic Nanoparticles for MRI Contrast Agents. *Adv Mater*. 2009; 21:2133–2148.
81. Muscas G, Singh G, Glomm WR, Mathieu R, Kumar PA, Concas G, Agostinelli E, Peddis D. Tuning the Size and Shape of Oxide Nanoparticles by Controlling Oxygen Content in the Reaction Environment: Morphological Analysis by Aspect Maps. *Chem Mater*. 2015; 27:1982–1990.
82. Rosensweig RE. Heating Magnetic Fluid with Alternating Magnetic Field. *J Magn Magn Mater*. 2002; 252:370–374.
83. Crowl DA. Minimize the Risks of Flammable Materials. *Chem Eng Prog*. 2012; 108:28–33.
84. Schneider CA, Rasband WS, Eliceiri KW. NIH Image to ImageJ: 25 Years of Image Analysis. *Nat Methods*. 2012; 9:671–675. [PubMed: 22930834]
85. Chen DX, Sanchez A, Taboada E, Roig A, Sun N, Gu HC. Size Determination Of Superparamagnetic Nanoparticles from Magnetization Curve. *J Appl Phys*. 2009:105.
86. Rasa M. Magnetic Properties and Magneto-Birefringence of Magnetic Fluids. *Eur Phys J E: Soft Matter Biol Phys*. 2000; 2:265–275.
87. Iglesias O, Labarta A, Batlle X. Exchange Bias Phenomenology and Models of Core/Shell Nanoparticles. *J Nanosci Nanotechnol*. 2008; 8:2761–2780. [PubMed: 18681014]
88. Goodwill PW, Tamrazian A, Croft LR, Lu CD, Johnson EM, Pidaparathi R, Ferguson RM, Khandhar AP, Krishnan KM, Conolly SM. Ferrohydrodynamic Relaxometry for Magnetic Particle Imaging. *Appl Phys Lett*. 2011; 98:262502.
89. Biederer S, Knopp T, Sattel TF, Ludtke-Buzug K, Gleich B, Weizenecker J, Borgert J, Buzug TM. Magnetization Response Spectroscopy of Superparamagnetic Nanoparticles for Magnetic Particle Imaging. *J Phys D: Appl Phys*. 2009; 42:205007.

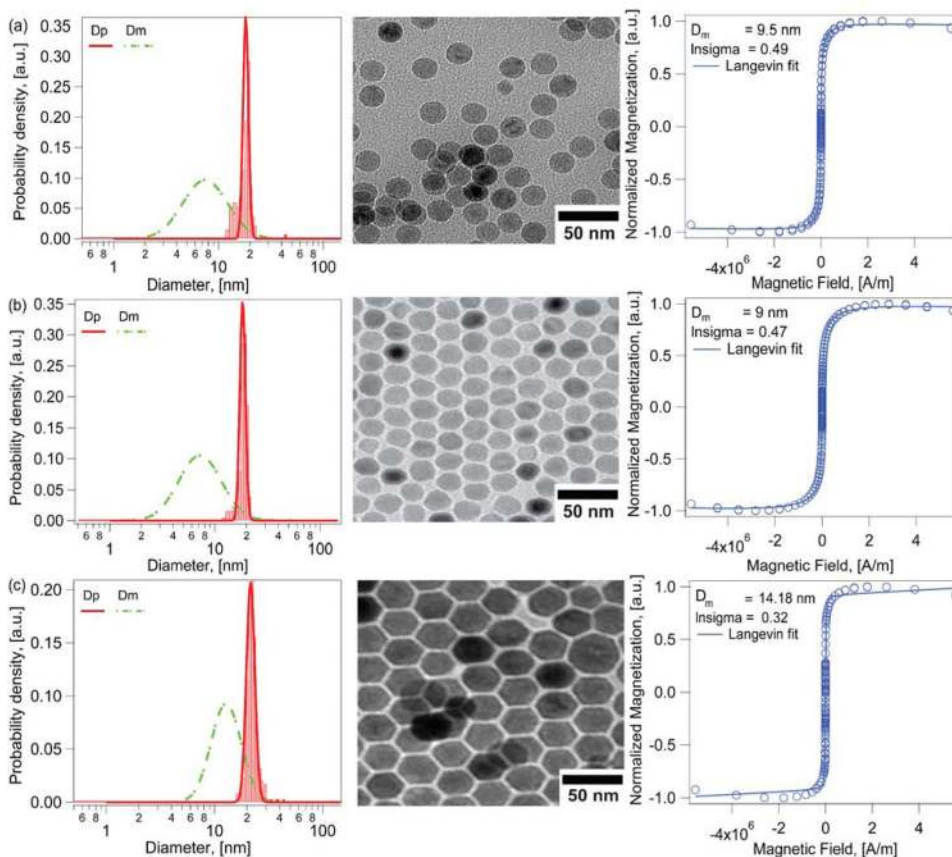


Figure 1.

Physical (red solid line) and magnetic (green dashed line) diameter distributions, representative transmission electron micrographs, and equilibrium magnetization curves for iron oxide nanoparticles obtained from two different thermal decomposition synthesis routes and commercially available nanoparticles from Ocean Nanotech, the corresponding TEM images and the Langevin fit to the equilibrium magnetization curves. a) Nanoparticles obtained from the heating-up thermal decomposition synthesis of an iron oleate precursor in trioctylamine at 350°C. b) Nanoparticles obtained by the Extended LaMer synthesis mechanism by dripping an iron oleate/1-octadecene precursor into a solvent system of oleic acid/docosane at 350°C. c) Commercial nanoparticles from Ocean Nanotech with a nominal diameter of 20 nm according to the manufacturer. Note how in all cases the magnetic diameter distributions are much smaller and much broader than the physical diameter distributions.

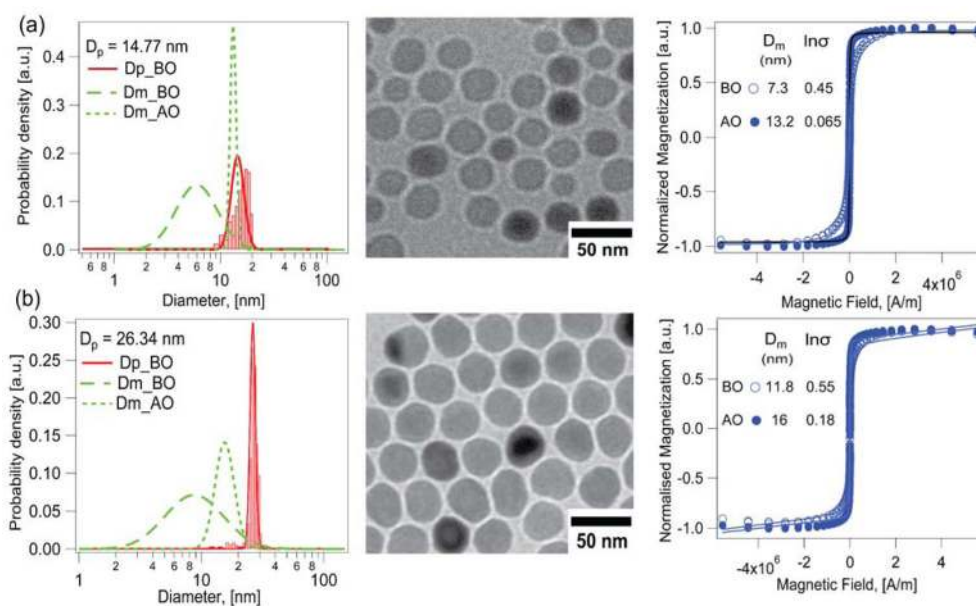


Figure 2.

Effect of post-synthesis thermal treatment on the magnetic diameter distribution for iron oxide nanoparticles obtained by the thermal decomposition synthesis under anaerobic conditions, for particles of two physical diameters. a) 14.77 nm b) 26.34 nm. The red solid line indicates the physical diameter distribution, which was relatively narrow for both nanoparticle samples. Green dashed lines indicate the magnetic diameter distributions before (BO, long dash) and after (AO, short dash) thermal treatment in an oxygen atmosphere for both samples. The corresponding TEM images and the Langevin fit to the equilibrium magnetization curves are laid out.

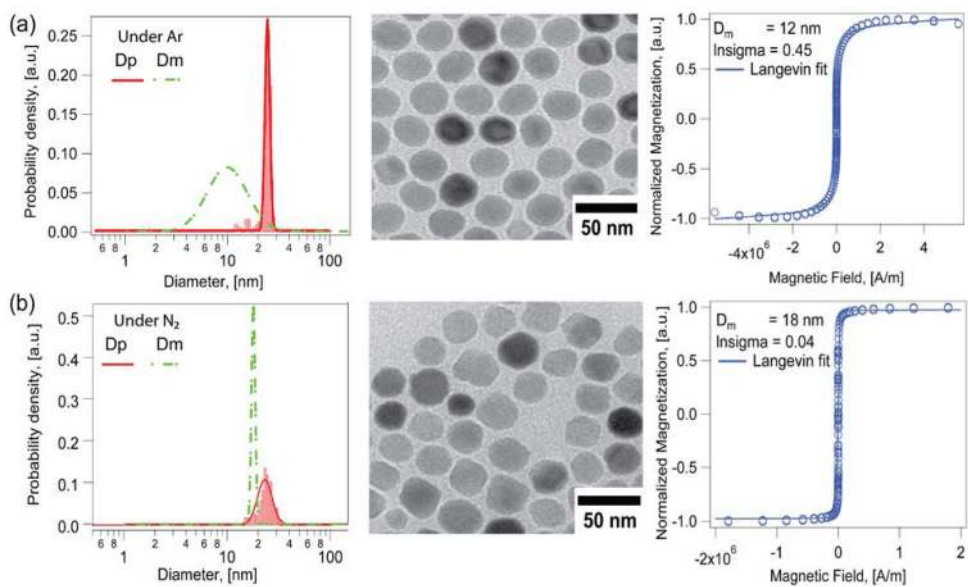


Figure 3. Physical (red solid line) and magnetic diameter (green dashed line) distributions for iron oxide nanoparticles obtained by the Extended LaMer mechanism based synthesis in the absence and presence of molecular oxygen and corresponding TEM images and the Langevin fit to the equilibrium magnetization curves for nanoparticles synthesized under a) Argon and b) Nitrogen atmosphere.

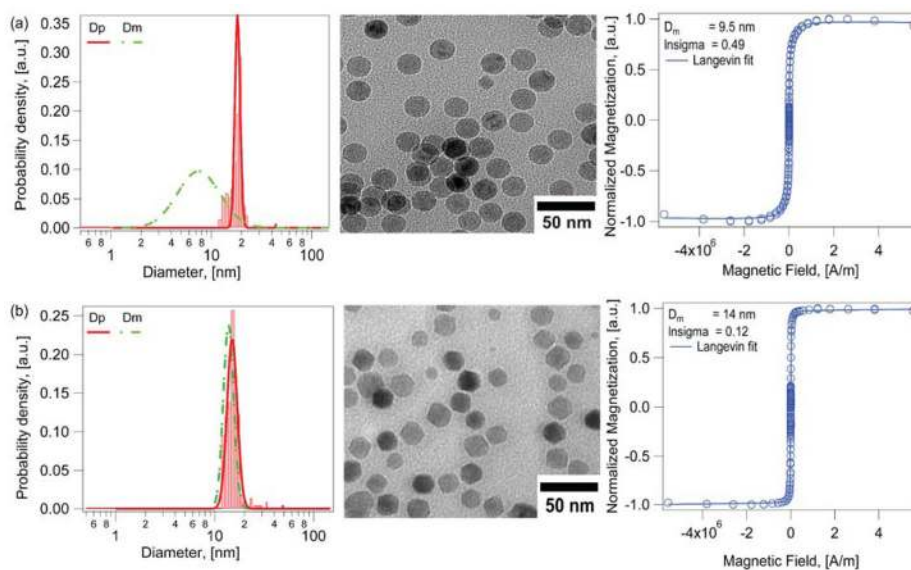


Figure 4. Effect of adding molecular oxygen on physical and magnetic diameters for iron oxide nanoparticles obtained by the heating up thermal decomposition synthesis. a) For particles synthesized in the absence of oxygen the magnetic diameter distribution (Green dashed line) is smaller and broader than the physical diameter distribution (Red solid line), b) For nanoparticles synthesized under identical conditions but with molecular oxygen added to the reactor the magnetic and physical diameters have similar distributions.

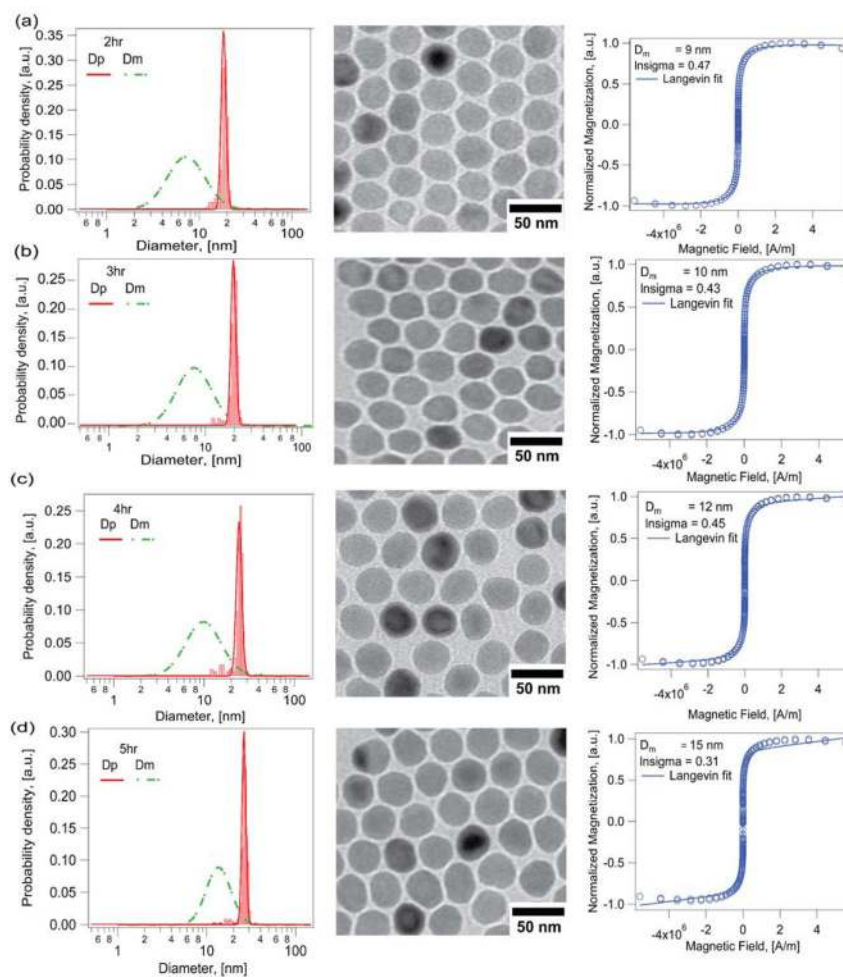


Figure 5. Controlled growth of physical but not magnetic diameter for iron oxide nanoparticles obtained using the Extended Lamer thermal decomposition synthesis in the absence of molecular oxygen for different time points of the reaction a) 2hr b) 3hr c) 4hr d) 5hr.

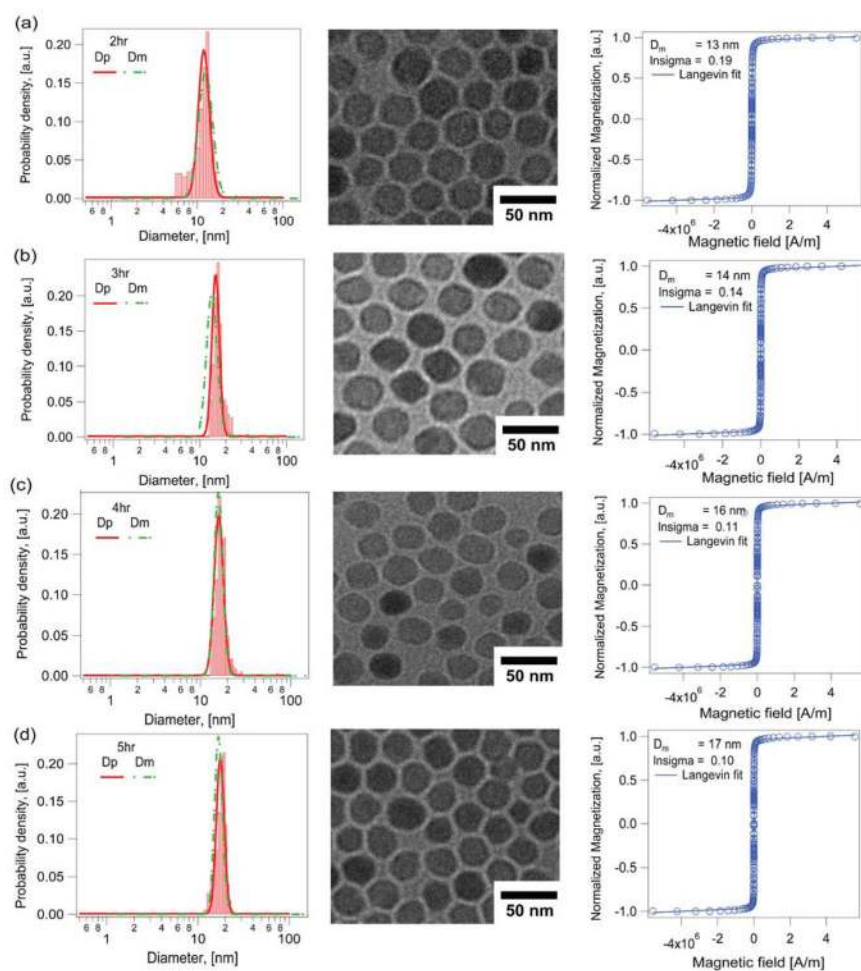


Figure 6. Controlled growth of both physical and magnetic diameter for iron oxide nanoparticles obtained using the Extended LaMer mechanism based synthesis thermal decomposition synthesis in the presence of molecular oxygen for different time points of the reaction a) 2hr b) 3hr c) 4hr d) 5hr.

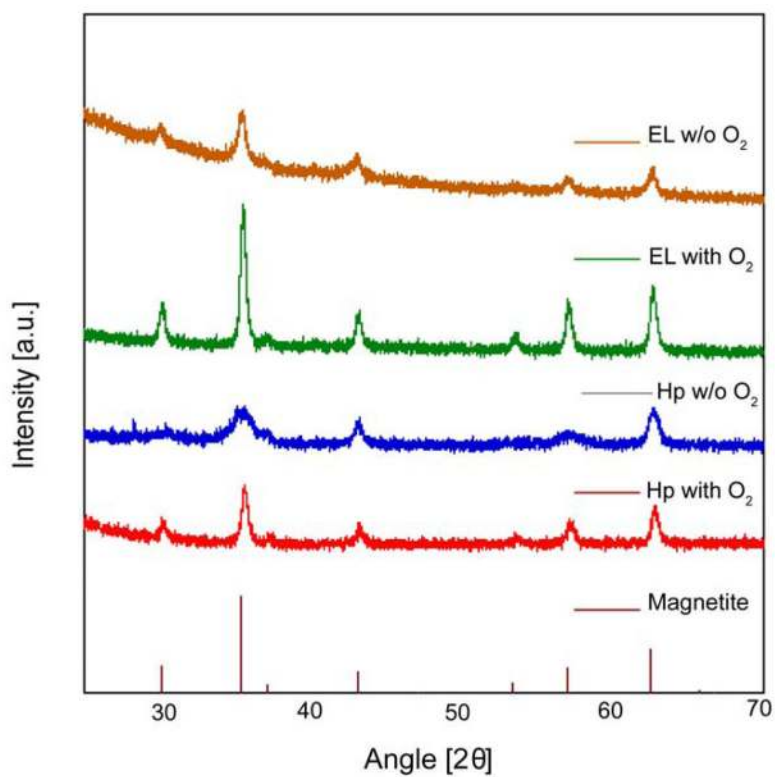


Figure 7. XRD powder diffractograms of iron oxide nanoparticles synthesized in the absence (w/o) and in the presence (with) of molecular oxygen (O_2) for both the Extended LaMer (EL) and heating up (Hp) method help understand the iron oxide phases present in the particle.

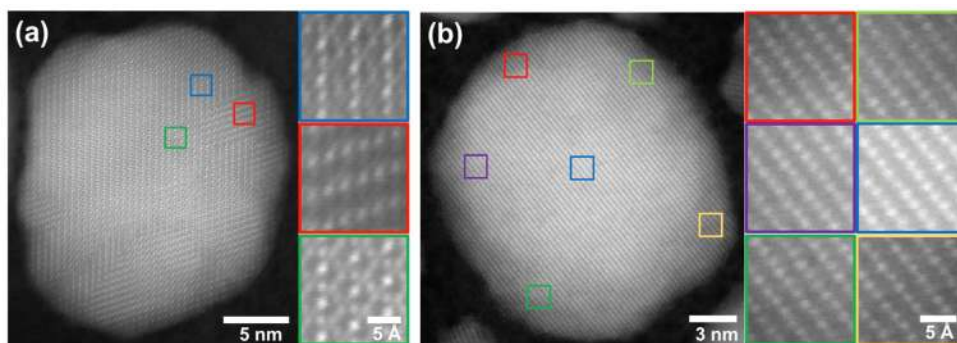


Figure 8. HAADF-STEM images of iron oxide nanoparticles synthesized (a) in the absence of oxygen show polycrystalline structure comprised of many smaller crystallites, highlighted in the high magnification insets. In contrast, nanoparticles synthesized (b) in the presence of oxygen show single crystal structure throughout the particles.

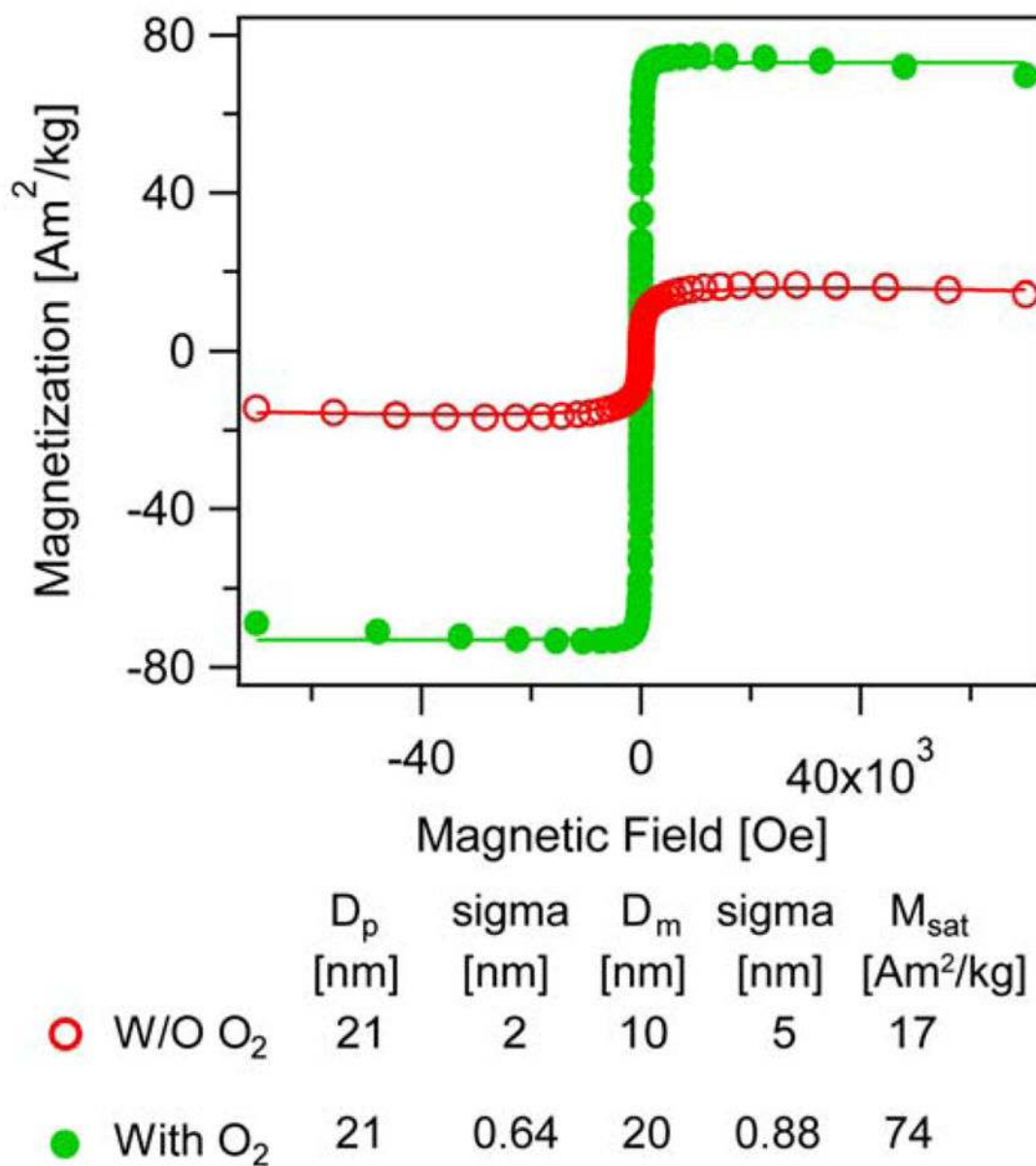


Figure 9. Saturation magnetization of iron oxide nanoparticles synthesized in the absence (red, open circles) and in the presence (green, closed circles) of molecular oxygen through the Extended LaMer thermal decomposition method.

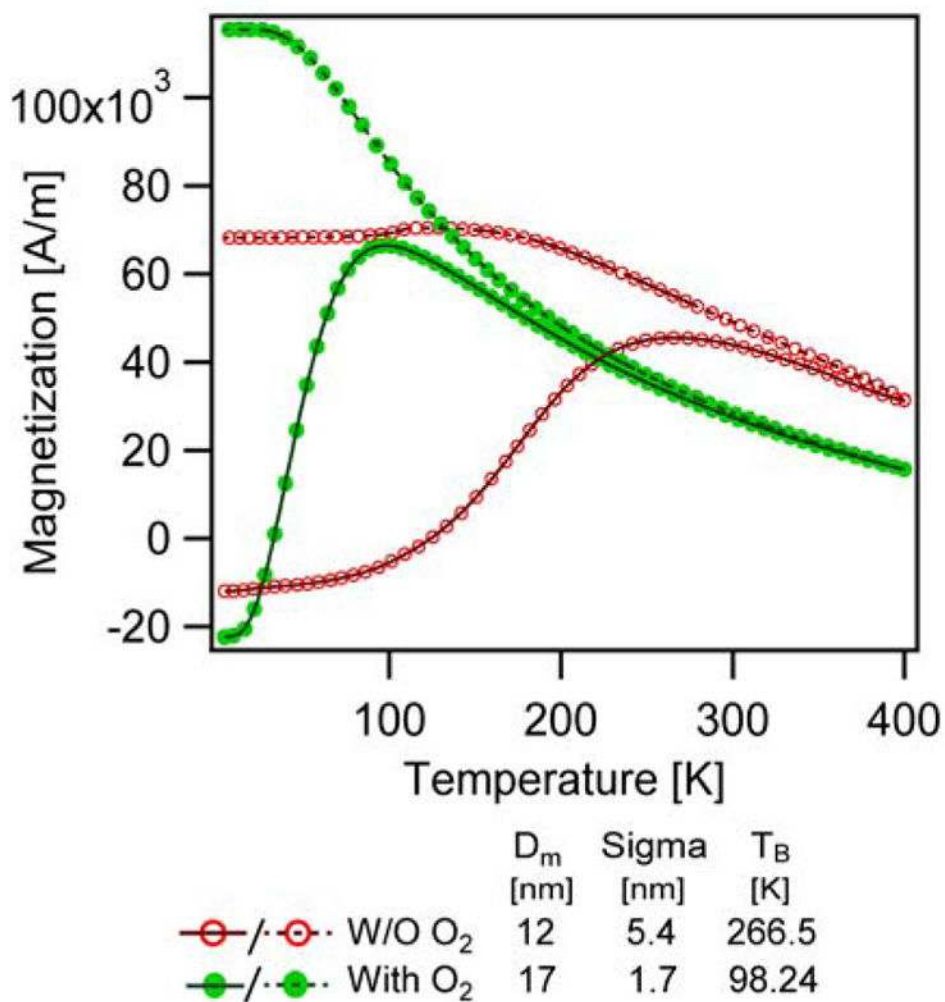


Figure 10. ZFC (solid line)-FC (dashed line) curves of the particles synthesized in the absence (red, open circles) and presence of oxygen (green, closed circles).

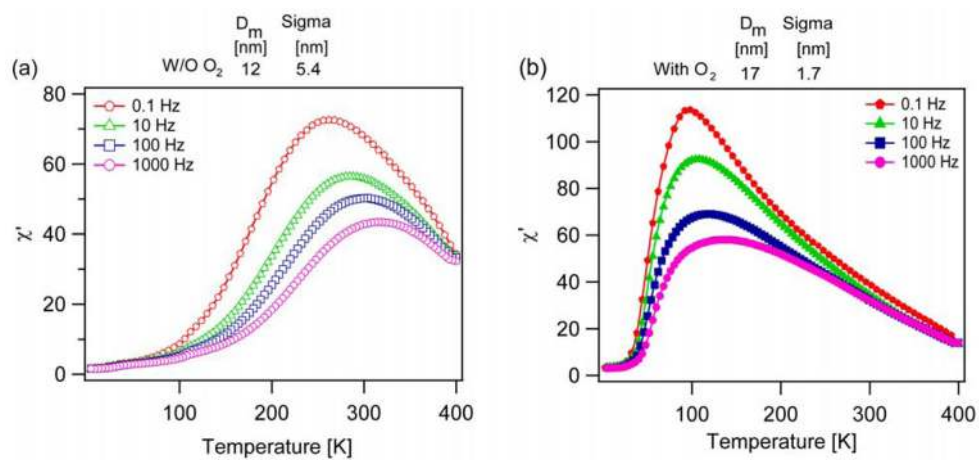


Figure 11. In-phase susceptibility vs temperature at different frequencies for particles synthesized a) without oxygen, b) with oxygen.

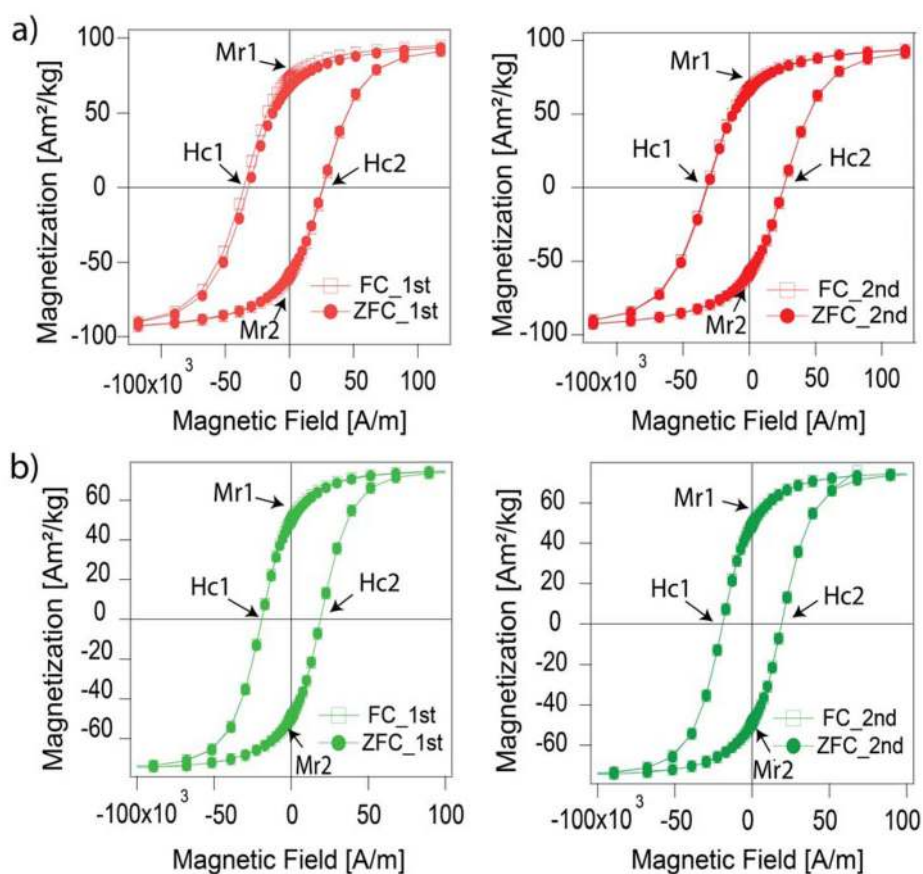


Figure 12.

Evidence of exchange bias in particles synthesized in the absence of oxygen (a) but not in particles synthesized in the presence of oxygen (b). FC – magnetization curves were obtained after cooling the sample from 298K to 5K in the presence of a 70 kOe magnetic field. ZFC – magnetization curves were obtained after cooling the sample from 298K to 5K in the absence of a magnetic field. The panels on the left show comparisons between magnetization curves obtained under FC and ZFC conditions after a single magnetization cycle. The panels on the right show comparisons between magnetization curves obtained under FC and ZFC conditions after a second magnetization cycle.

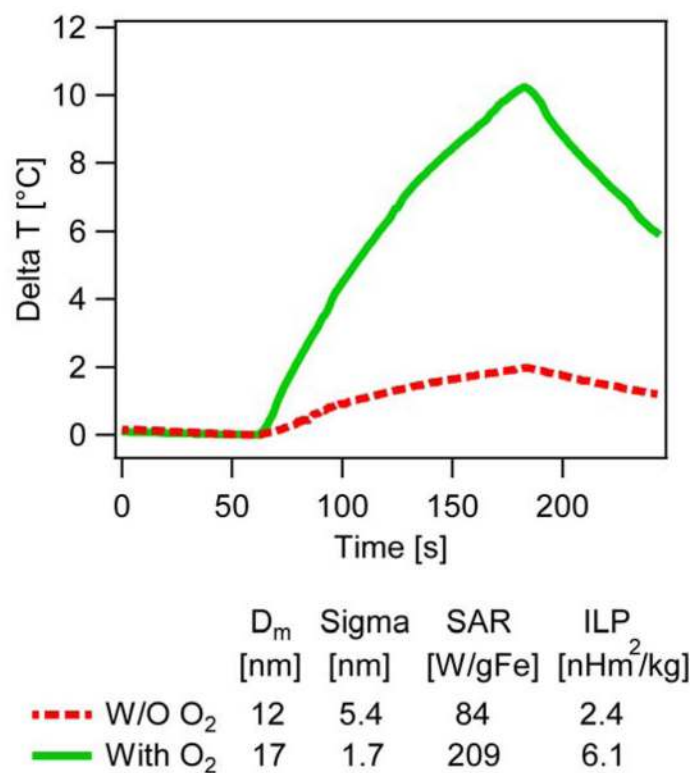


Figure 13.

Comparison of thermal energy dissipation by magnetic nanoparticles in alternating magnetic fields for nanoparticles synthesized in the absence (red, dashed line) and presence of oxygen (green, solid line)

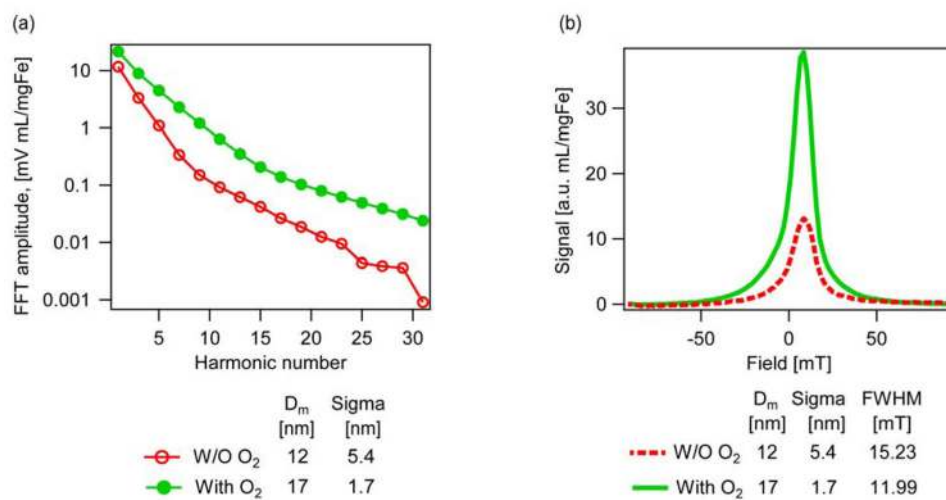


Figure 14. Comparison of a) FFT amplitude as a function of Harmonic number, b) point spread function of the particles synthesized in the presence and absence of oxygen.

Comparison of physical, magnetic, and crystallite sizes for iron oxide nanoparticles obtained by the heating up and Extended LaMer thermal decomposition syntheses in the absence and in the presence of oxygen.

Table 1

Method	D_p (nm)	σ_p (nm)	D_m (nm)	σ_m (nm)	D_{XRD} (nm)
Extended LaMer Without O ₂	26.0	1.3	15.7	5.1	15.8
Extended LaMer With O ₂	24.1	2.9	23.0	0.5	22.0
Heating up Without O ₂	18.5	1.7	10.7	5.6	10.8
Heating up With O ₂	15.4	1.9	14.1	1.7	14.7